J. Fluid Mech. (2023), *vol*. 967, A8, doi:10.1017/jfm.2023.459

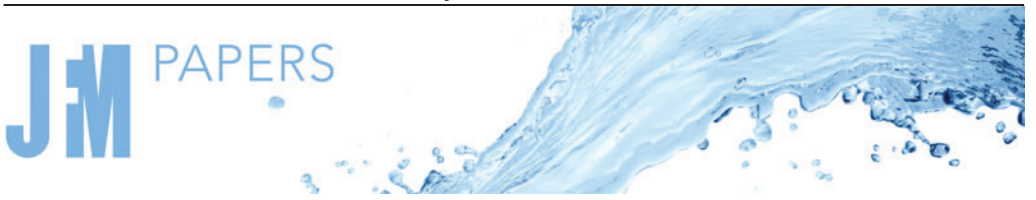

How electrostatic forces affect particle behaviour in turbulent channel flows

Huan Zhang[1], **Yuankai Cui**[1] **and Xiaojing Zheng**[2,†]

[1]Center for Particle-laden Turbulence, Lanzhou University, Lanzhou 730000, PR China

[2]Research Center for Applied Mechanics, Xidian University, Xi'an 710071, PR China

(Received 12 September 2022; revised 5 April 2023; accepted 26 May 2023)

In dispersed two-phase flows, particle electrification is a prevalent phenomenon that plays a crucial role in particle transport. However, the influences of electrostatic forces on particle behaviour in wall-bounded turbulent flows, especially in bidisperse cases, is not well understood. In this study, using direct numerical simulations based on a coupled Eulerian–Lagrangian point-particle approach at friction Reynolds number $Re_\tau = 550$, we demonstrate that when the electrostatic Stokes number is of the order of $O(10^{-1})$, electrostatic forces could considerably alter particle behaviour in both monodisperse and bidisperse particle-laden turbulent channel flows. Specifically, the wall-normal profiles of the particle concentration are determined by the competition of turbophoresis, biased sampling and electrostatic effects. The electrostatic forces are found to reduce the concentrations of lighter particles by electrostatic drift directly, whereas they alter those of heavier particles by strengthening turbophoresis indirectly. With increasing electrical charge, the dynamics of the lighter particles remains approximately unchanged, but that of the heavier particles is modulated significantly due to their relatively strong particle–electrostatic interaction. In the near-wall region, electrostatic forces tend to homogenize the distribution of lighter particles in the spanwise direction by inhibiting the formation and destruction of particle clusterings and voids, thereby maintaining the anisotropic streaky clusterings. Furthermore, even though the clustering dynamics remains unchanged, the spatial extents of the clusterings at the channel centreline are suppressed (enhanced) by a factor of two, probably due to the remarkable reduction (increase) of particle concentration in this layer.

Key words: particle/fluid flow

1. Introduction

Particle electrification is ubiquitous in disperse two-phase flows, such as fluidized beds (Sippola *et al.* 2018) and pneumatic powder transports (Nifuku & Katoh 2003; Grosshans

† Email address for correspondence: xjzheng@lzu.edu.cn

& Papalexandris 2016) in industrial processes, and sand saltation (Schmidt, Schmidt & Dent 1998; Zheng, Huang & Zhou 2003), dust storms (Yair *et al.* 2016; Zhang & Zheng 2018; Zhang & Zhou 2020, 2023) and volcanic eruptions (Mather & Harrison 2006; Méndez Harper & Dufek 2016) in atmospheric flows. Field and laboratory measurements regarding these phenomena have shown that the mean electric field produced by charged particles can reach strengths of several hundred kilovolts per metre, so that the inter-particle electrostatic force is comparable with the particle's gravitational force and thus affects the particle behaviour considerably (Renno & Kok 2008). In particular, electrostatic force is found to facilitate the aerodynamic lifting of particles from the surface, by reducing the threshold friction velocity necessary to initiate particle lifting (e.g. Kok & Renno 2006). Also, electrostatic force tends to enhance saltation mass flux when particles are negatively charged but inhibit the mass flux when particles are positively charged (Zheng *et al.* 2003). Even though particle electrification has been observed and investigated for more than 100 years in natural conditions (e.g. Rudge 1913), it is not well understood because of the strong particle–turbulence and particle–electrostatics interphase couplings (e.g. Zheng 2013).

In wall-bounded turbulent flows laden with uncharged inertial particles, there is a tendency for particles to migrate towards the wall (i.e. the direction of negative gradient of turbulence intensity), resulting in a peak in mean particle concentration within the viscous layer, which is known as turbophoresis (Caporaloni *et al.* 1975; Reeks 1983). This particle migration is thought to be most pronounced when the particle response time scale matches the characteristic time scale of the buffer layer (Soldati & Marchioli 2009; Sardina *et al.* 2012; Lee & Moser 2015). Furthermore, it is well recognized that in low-Reynolds-number turbulent flows (typically with friction Reynolds number $Re_\tau \sim O(10^2)$; see § 2.1 for the definition), inertial particles tend to aggregate preferentially into the regions of lower-than-mean streamwise velocity in the wall region, referred to as preferential concentration, which forms small-scale streak-like particle clustering and thus very non-uniform local particle concentration (e.g. Pedinotti, Mariotti & Banerjee 1992; Eaton & Fessler 1994; Pan & Banerjee 1996; Marchioli & Soldati 2002; Sardina *et al.* 2012). Such a small-scale streaky clustering is maximized when the particle response time scale is of the order of the Kolmogorov time scale (i.e. intermediate-inertia particles). For small- and large-inertia particles (i.e. particle response time scale much smaller or larger than the Kolmogorov time scale), they cannot form clustering, because the former particles follow the fluid faithfully, and the latter ones are almost independent of the flow. Note that in high-Reynolds-number turbulent flows (with $Re_\tau \gtrsim O(10^3)$), besides small-scale clustering for intermediate-inertia particles, large-scale clustering for the relatively large-inertia particles is present due to the presence of large-scale fluid motions (Oka & Goto 2021; Jie *et al.* 2022; Motoori, Wong & Goto 2022). In fact, particle transfer in the wall region is dominated by the coherent sweep and ejection events, where the former carry particles towards the wall, while the latter bring particles away from the wall (Marchioli & Soldati 2002). Since only a fraction of particles that are entrained into the viscous sublayer by sweeps can be re-entrained towards the outer layer by ejections, the particle flux towards the wall is larger than the particle flux away from the wall, resulting in non-uniform distribution and near-wall accumulation of particles (Soldati & Marchioli 2009; Sardina *et al.* 2012; Costa, Brandt & Picano 2020; Brandt & Coletti 2022).

It is expected that when particles are electrically charged, their behaviour could be altered considerably. Although particle electrification has been neglected for a long time in the study of particle-laden turbulent flows, it has continued to attract a lot of attention

in the last two decades, due to recent advances in experimental facilities and direct numerical simulations (DNS). A large number of existing works focus on the influences of electrostatic forces on particle clustering in homogeneous isotropic turbulence (HIT). For monodisperse like-charged particles in HIT, Alipchenkov, Zaichik & Petrov (2004) proposed a statistical model based on the kinetic equation of the relative velocity of particle pairs, and revealed that clustering is suppressed appreciably. This mitigation of preferential concentration is confirmed adequately by subsequent DNS and laboratory experiments (e.g. Lu *et al.* 2010; Karnik & Shrimpton 2012; Lu & Shaw 2015; Yao & Capecelatro 2018). More recently, a DNS study by Boutsikakis, Fede & Simonin (2022) found that electrostatic forces could inhibit the dispersion of like-charged particles in HIT, by decreasing the correlation between particle velocity and fluid acceleration, and destroying the particle–fluid covariance. In addition to monodisperse particles, Di Renzo & Urzay (2018) have investigated bidisperse oppositely charged particles in HIT that are widely encountered but poorly understood in actual conditions. They showed that when electrostatic forces are mild, the small-inertia negatively charged particles are aggregated preferentially into low-vorticity high-strain fluid regions, while the large-inertia positively charged particles are distributed randomly, leading to charge separation according to particle inertia (e.g. Cimarelli *et al.* 2014; Zhang & Zhou 2020). By contrast, when electrostatic forces are severe, the small-inertia negatively charged particles become more uniformly distributed and indistinguishable from the large-inertia positively charged particles. It is worth noting that these DNS works have not incorporated particle–turbulence two-way coupling and inter-particle collisions, but the two effects are believed to be significant even at relatively low bulk particle volume fractions (e.g. Wang, Wexler & Zhou 2000; Sardina *et al.* 2012; Costa *et al.* 2020; Johnson 2020), because turbophoresis and clustering cause locally very high concentration and mass loading. Until now, only Grosshans and co-workers have studied the role of electrostatic forces in wall turbulence by DNS (e.g. Grosshans *et al.* 2021). They simulated monodisperse charged particles in turbulent duct flows and demonstrated that electrostatic forces dramatically suppress both the vortical motion of particles and particle–fluid streamwise momentum transfer. However, when considering particle–turbulence and particle–electrostatics interphase couplings, as well as inter-particle collisions, the distribution, dynamics and clustering of particles in the wall region discussed above are still largely unclear, especially for bidisperse flows. Specifically, do the electrostatic forces play a role in the particle-laden turbulent channel flows? How do the electrostatic forces influence particle behaviour? What are the underlying physical mechanisms responsible for the electrostatic effects?

In this study, the main aims are twofold: (1) to quantify the role of electrostatic forces in the behaviour of the monodisperse and bidisperse particles embedded in low-Reynolds-number turbulent channel flows; and (2) to unveil the underlying physical mechanism responsible for the electrostatic effects. For these purposes, we perform a series of DNS of turbulent channel flows at $Re_\tau = 550$ laden with both monodisperse and bidisperse charged particles, in which the particle–turbulence and particle–electrostatics two-way couplings, as well as inter-particle collisions, are taken into account explicitly. The paper is organized as follows. First, the numerical model is described in §§ 2.1–2.3, and simulation set-up and verification are provided in detail in § 2.4 and Appendix A, respectively. Second, the roles of electrostatic forces in particles' distribution, dynamics and clustering are discussed in §§ 3.1, 3.2 and 3.3, respectively. Finally, conclusions and an outlook on future work are given in § 4.

2. Numerical methodology

2.1. *Turbulent channel flow*

We simulate the aforementioned particle-laden turbulent channel flows using a coupled Eulerian–Lagrangian point-particle approach supplemented with electrostatic equations, since the particles considered herein are dilute suspension and small compared to the Kolmogorov scale (e.g. Maxey & Riley 1983; Maxey 1987; Balachandar 2009). In such a case, the incompressible Newtonian carrier fluid is governed by the mass and momentum balance equations as

$$\boldsymbol{\nabla} \cdot \boldsymbol{u} = 0, \tag{2.1}$$

$$\frac{\partial \boldsymbol{u}}{\partial t} + (\boldsymbol{u} \cdot \boldsymbol{\nabla})\boldsymbol{u} = -\frac{1}{\rho_f}\boldsymbol{\nabla} p + \nu \nabla^2 \boldsymbol{u} + \boldsymbol{f}, \tag{2.2}$$

where $\boldsymbol{u} = (u, v, w)$ and $\boldsymbol{x} = (x, y, z)$ represent the fluid velocity and spatial coordinate, respectively, with u, v and w (x, y and z) being the streamwise, wall-normal and spanwise velocities (coordinates). In addition, t stands for the physical time, and ρ_f, p and ν denote the fluid density, pressure and kinematic viscosity, respectively. The source term $\boldsymbol{f}$ is added to account for the feedback force exerted by the particles on the fluid, which is calculated as (Marshall 2009; Zhao, Andersson & Gillissen 2013; Zheng, Feng & Wang 2021)

$$\boldsymbol{f} = -\frac{1}{\rho_f V_{cell}} \sum_{k=1}^{n_p} \boldsymbol{f}_D^k. \tag{2.3}$$

Here, $\boldsymbol{f}_D^k$ is the hydrodynamic drag force acting on the kth particle within a computational cell of volume V_{cell} containing n_p particles.

We consider turbulent channel flow that is driven by a uniform pressure gradient, such that a constant bulk velocity is maintained. The dimensionless control parameter, i.e. the friction Reynolds number, is defined as $Re_\tau = u_\tau \delta/\nu$, where u_τ is the friction velocity, and δ is the channel half-width. Throughout this paper, the superscript $+$ denotes quantities that are normalized based on u_τ and ν (i.e. in viscous or wall units, such as time $\tau_\nu = \nu/u_\tau^2$ and length $\delta_\nu = \nu/u_\tau$ scales). Periodic boundary conditions in the horizontal (i.e. streamwise and spanwise) directions and no-slip boundary conditions at the wall are employed. Equations (2.1) and (2.2) are solved based on the canonical Navier–Stokes solver (CaNS) developed by Costa (2018), using a fast Fourier transform (FFT) based pressure correction method (Kim & Moin 1985). A standard second-order central finite-difference scheme is used for the space discretization on a staggered Cartesian mesh. Time is advanced with a third-order Runge–Kutta scheme. The solution of the Poisson equation for the pressure correction is based on the eigenfunction expansion method (Schumann & Sweet 1988). The FFT-based expansions are employed in the horizontal, uniformly discretized directions, then Gaussian elimination is used to solve the resulting tridiagonal system along the wall-normal direction.

2.2. *Lagrangian particle tracking*

For the particulate phase, we consider small, rigid, charged or uncharged, and spherical particles that are suspended in the turbulent channel flow. The particle density ρ_p (particle diameter d_p) is taken to be much larger than ρ_f (smaller than the Kolmogorov scale), so that the point-particle approximation is quite reasonable and the Stokes drag force

is the dominant hydrodynamic force on the particle (Maxey & Riley 1983; Armenio & Fiorotto 2001; Balachandar & Eaton 2010). To emphasize the effects of particle inertia and electrostatic forces, gravitational settling is not taken into account (e.g. Wang & Richter 2019; Jie *et al.* 2022; Motoori *et al.* 2022). Consequently, in the Lagrangian description, each particle is tracked individually using the governing equations as

$$\frac{\mathrm{d}\boldsymbol{x}_p}{\mathrm{d}t} = \boldsymbol{u}_p, \tag{2.4}$$

$$\frac{\mathrm{d}\boldsymbol{u}_p}{\mathrm{d}t} = \frac{\zeta}{\tau_p}\left(\boldsymbol{u}_{f@p} - \boldsymbol{u}_p\right) + \frac{q\boldsymbol{E}_{@p}}{m_p}, \tag{2.5}$$

where $\boldsymbol{x}_p$ is the particle position, $\boldsymbol{u}_p$ is the particle velocity, $\zeta = 1 + 0.15\,Re_p^{0.687}$ with $Re_p = d_p\,|\boldsymbol{u}_{f@p} - \boldsymbol{u}_p|/\nu$ being the particle Reynolds number (Schiller & Naumann 1935; Lavrinenko, Fabregat & Pallares 2022), $\tau_p = d_p^2\rho_p/(18\nu\rho_f)$ is the particle inertial response time (e.g. Maxey 1987; Eaton & Fessler 1994), $\boldsymbol{u}_{f@p}$ is the fluid velocity at the particle position, q is the electric charge of the particle, $\boldsymbol{E}_{@p}$ is the electric field at the particle position, and $m_p = \pi\rho_p d_p^3/6$ is the particle mass.

From (2.5), there are two dimensionless parameters controlling the particle dynamics. One is the viscous (or Kolmogorov) aerodynamic Stokes number $St^+ = \tau_p/\tau_\nu$ ($St_k = \tau_p/\tau_\eta$), which is defined as the ratio of the particle inertial response time τ_p to the viscous time scale τ_ν (Kolmogorov time scale τ_η). The other parameter, termed the electrostatic Stokes number, is defined as $St_{el} = \tau_p/\tau_{el}$, where $\tau_{el} = (6\pi\varepsilon_0 m_p/(nq^2))^{1/2}$ stands for the characteristic time scale of the inter-particle electrostatic interactions (Boutsikakis *et al.* 2022), with n and ε_0 being the particle number density and the permittivity of the vacuum, respectively. The two parameters weigh the importance of particle inertia and electrostatic forces. In particular, particles will attain a ballistic motion when the aerodynamic Stokes number is much larger than unity, but become tracers when the aerodynamic Stokes number is much smaller than unity. Also, the inter-particle electrostatic forces are dominating (negligible) if the electrostatic Stokes number is much larger (smaller) than unity.

Similarly, we impose periodic boundary conditions for particles in the horizontal directions, and reflective boundary conditions for particles on the top and bottom walls. A particle–wall collision occurs when the distance between the particle centre and the wall is less than the particle radius. Inter-particle collisions are also taken into account since preferential concentration and turbophoresis lead to a locally very high particle concentration (e.g. Wang *et al.* 2000; Yamamoto *et al.* 2001). Unless stated otherwise, both particle–wall and inter-particle collisions are assumed to be fully elastic (thus conserving kinetic energy) and are described using the 'hard-sphere' approach, as in many previous studies (e.g. Marchioli & Soldati 2002; Sardina *et al.* 2012; Johnson, Bassenne & Moin 2020; Motoori *et al.* 2022). Therefore, when colliding with the wall, the tangential velocity of the particle remains unchanged and the wall-normal component is of the same magnitude but opposite direction (i.e. reflective). Notably, particle collisions in a viscous fluid are actually inelastic, with restitution coefficient smaller than unity (e.g. Rice, Willetts & McEwan 1995; Joseph *et al.* 2001; Gondret, Lance & Petit 2002; Yang & Hunt 2006). However, the differences in the results between inelastic and elastic collisions considered herein are found to be negligible (e.g. Sardina *et al.* 2012; Johnson *et al.* 2020).

Only binary inter-particle collisions are considered due to dilute particle loading. Thus, considering that two particles labelled as 1 and 2 with velocities $\boldsymbol{u}_{p,1}$ and $\boldsymbol{u}_{p,2}$ collide with

each other, the post-collision velocity of particle 1 is given by (Grosshans & Papalexandris 2017*a*)

$$\boldsymbol{u}_{p,1}^{post} = \frac{\boldsymbol{u}_{p,1}(m_{p,1} - m_{p,2}) + 2m_{p,2}\boldsymbol{u}_{p,2}}{m_{p,1} + m_{p,2}}, \tag{2.6}$$

where $m_{p,1}$ and $m_{p,2}$ are the masses of particles 1 and 2, respectively. For particle 2, post-collision velocity is obtained by permutation of the indices 1 and 2.

Time integration of (2.4) and (2.5) is performed using a fourth-order Runge–Kutta scheme. Inter-particle collisions are detected by the Eulerian-mesh-based method, in which the potential colliding particle pairs are found in the target and its neighbouring cells (for the details, see Capecelatro & Desjardins 2013).

2.3. *Electric fields*

The electric field at each particle position is calculated by the particle-particle-particle-mesh (P^3M) method, encompassing long-range component accounting for far-field effects, short-range component accounting for neighbouring particles, and a correction term to exclude double counting of the former two (Kolehmainen *et al.* 2016; Grosshans & Papalexandris 2017*b*; Sippola *et al.* 2018). Considering particle i located at $\boldsymbol{x}_i$, the long-range component $\boldsymbol{E}_{\nabla^2}$ can be determined by projecting particles to the computational mesh and solving the Poisson equation for the electrical potential:

$$\nabla^2\varphi = -\frac{\rho_e}{\varepsilon_0}, \tag{2.7}$$

$$\boldsymbol{E}_{\nabla^2} = -\nabla\varphi, \tag{2.8}$$

where φ is the electric potential, and $\rho_e = \sum_{k=1}^{n_p} q_k/V_{cell}$ is the space-charge density. Note that this Eulerian formulation has been used solely for quantifying the electrostatic forces acting on particles through interpolation, as in Karnik & Shrimpton (2012), Kolehmainen, Ozel & Sundaresan (2018) and Grosshans *et al.* (2021). Again, the periodic boundary conditions are applied to electrical potential in the horizontal directions, but zero-Dirichlet conditions ($\varphi = 0$) are set at the wall. Equation (2.7) is resolved by the same algorithm as used for the Poisson equation of pressure correction.

As done in Sippola *et al.* (2018), the short-range component $\boldsymbol{E}_{s,i}$ for particle i within computational cell A is determined directly by Coulomb's law

$$\boldsymbol{E}_{s,i} = \frac{1}{4\pi\varepsilon_0}\sum_{j\neq i} q_j \frac{\boldsymbol{x}_i - \boldsymbol{x}_j}{|\boldsymbol{x}_i - \boldsymbol{x}_j|^3}, \tag{2.9}$$

where the sum is taken over all neighbouring particles j carrying charge q_j located in cell A and its adjacent cells.

To avoid double counting of the overlap of long- and short-range components, a correction term is introduced as

$$\boldsymbol{E}_{c,A} = -\frac{1}{4\pi\varepsilon_0}\sum_{B\neq A} Q_B \frac{\boldsymbol{x}_A - \boldsymbol{x}_B}{|\boldsymbol{x}_A - \boldsymbol{x}_B|^3}, \tag{2.10}$$

where the sum is performed over all adjacent cells B of cell A, Q_B is the total charge enclosed within cell B, and $\boldsymbol{x}_A$ and $\boldsymbol{x}_B$ are the coordinates of the centre of the cell.

Re_τ	$L_x \times L_y \times L_z$	$N_x \times N_y \times N_z$	Δx_g^+	Δy_g^+	Δz_g^+
550	$2\pi\delta \times 2\delta \times \pi\delta$	$384 \times 384 \times 256$	9.00	0.43–4.75	6.75

Table 1. Grid parameters for the DNS. Here, L_x, L_y and L_z are the streamwise, wall-normal and spanwise computational domain sizes, respectively, $\delta = 0.2$ m is the channel half-width, N_x, N_y and N_z are the numbers of grid points, and Δx_g^+, Δy_g^+ and Δz_g^+ are the grid spacings normalized by the viscous length scale ν/u_τ.

2.4. *Simulation set-up*

The simulations to be discussed in the present study are performed at $Re_\tau = 550$. The computational domain is set as $2\pi\delta \times 2\delta \times \pi\delta$, which is large enough to capture accurately particle behaviours even at Re_τ from 1000 to 5186 (Jie *et al.* 2022; Motoori *et al.* 2022; Gao, Samtaney & Richter 2023). Detailed information on the selection of such a computational domain can be found in Gao *et al.* (2023). A total of $384 \times 384 \times 256$ grid points are used to discretize the computational domain. The grid spacing is uniform in the horizontal directions, with $\Delta x_g^+ \approx 9.00$ and $\Delta z_g^+ \approx 6.75$. However, a stretched grid is used to refine the grid close to the wall, thus Δy_g^+ varies approximately from 0.43 to 4.75. The grid parameters are summarized in table 1.

To uncover the effects of electrostatic forces on particle behaviour, we consider both monodisperse and bidisperse particles embedded in the turbulent channel flows with five different electrostatic Stokes numbers, as shown in table 2. For the monodisperse cases, the aerodynamic number is specified as $St^+ = 20$, at which the near-wall particle streaks are very prominent. In each case, a total number of $N = 2 \times 10^6$ particles carry an identical electrical charge q ranging from 0 to -0.01 pC, corresponding to the bulk mean electrostatic Stokes number in the range $\overline{St_{el}} \in [0, 0.59 \times 10^{-2}]$. By contrast, two classes of particles are examined in the bidisperse cases, where the lighter particles, $St^+ = 20$, are negatively charged, while the heavier ones, $St^+ = 400$, are positively charged with equal magnitude (from 0 to 0.1 pC). As a result, the bulk mean electrostatic Stokes number $\overline{St_{el}}$ varies from 0 to 4.14×10^{-2} (0 to 1.85×10^{-1}) for the lighter (heavier) particles. These $\overline{St_{el}}$ values are of the same order as those used in Di Renzo *et al.* (2019) and Grosshans *et al.* (2021), but one order of magnitude smaller than those used in Boutsikakis *et al.* (2022). The given maximum electrical charge (i.e. 0.1 pC) is approximately a quarter of the saturation charge on the particles $q_s = 0.44$ pC ($q_s = \pi d_p^2 E_{sat} \varepsilon_0$), which is limited by the dielectric breakdown of the carrier fluid with breakdown field strength $E_{sat} = 3 \times 10^3$ kV m^{-1} (e.g. Hamamoto, Nakajima & Sato 1992). Note that charge exchanges during inter-particle and particle–wall collisions are not taken into account, as done by Di Renzo & Urzay (2018), Grosshans *et al.* (2021) and Boutsikakis *et al.* (2022). This is because there is no consensus on how the electrical charge is distributed among particles, which is very sensitive to the selection of charge exchange model (Lacks & Sankaran 2011). The bidisperse particles are equally repartitioned among the two classes (i.e. 1×10^6 particles for each class), keeping the system electrically neutral (Di Renzo & Urzay 2018). The particle diameters considered in both monodisperse and bidisperse cases are fixed at $d_p^+ = 0.2$ (i.e. $d_p = 72.7$ μm), which is smaller than the Kolmogorov length scales of the simulated flows and the minimum grid spacing $\Delta y_{min}^+ \approx 0.43$, so the point-particle approach is applicable (Horwitz & Mani 2016). Accordingly, the particle-to-fluid density ratio is $\rho_p/\rho_f = 9 \times 10^3$ for the lighter particles, and $\rho_p/\rho_f = 1.8 \times 10^5$ for the heavier particles. It is noteworthy that even though such large particle-to-fluid density ratios

Case	Re_τ	$\overline{\phi_m}$ ($\times 10^{-2}$)	$\overline{\phi_v}$ ($\times 10^{-6}$)	St^+	$St_{k,max}$	$St_{k,min}$	q (pC)	$\overline{St_{el}}$ ($\times 10^{-2}$)
MD0	550	1.14	1.28	20	4.84	0.51	0	0
MD0.001	550	1.14	1.28	20	4.84	0.51	−0.001	0.06
MD0.003	550	1.14	1.28	20	4.84	0.51	−0.003	0.18
MD0.006	550	1.14	1.28	20	4.84	0.51	−0.006	0.35
MD0.01	550	1.14	1.28	20	4.84	0.51	−0.01	0.59
BD0	550	0.57, 11.4	0.64, 0.64	20, 400	4.84, 96.8	0.51, 10.1	0	0
BD$^{\pm}$0.006	550	0.57, 11.4	0.64, 0.64	20, 400	4.84, 96.8	0.51, 10.1	−0.006, 0.006	0.25, 1.11
BD$^{\pm}$0.01	550	0.57, 11.4	0.64, 0.64	20, 400	4.84, 96.8	0.51, 10.1	−0.01, 0.01	0.41, 1.85
BD$^{\pm}$0.02	550	0.57, 11.4	0.64, 0.64	20, 400	4.84, 96.8	0.51, 10.1	−0.02, 0.02	0.83, 3.70
BD$^{\pm}$0.1	550	0.57, 11.4	0.64, 0.64	20, 400	4.84, 96.8	0.51, 10.1	−0.1, 0.1	4.14, 18.5

Table 2. Main parameters for the particles. Here, $\overline{\phi_m}$, $\overline{\phi_v}$ and $\overline{St_{el}}$ represent the bulk mean particle mass loading ratio, particle volume fraction and electrostatic Stokes number, respectively. The particle Stokes numbers St^+ and St_k are calculated based on the viscous and Kolmogorov time scales, respectively, where the subscript max (min) refers to the maximum (minimum) St_k at the wall (channel centreline).

are rarely encountered in natural phenomena, the particles with the same controlling parameters (St^+ and St_{el}) at common density ratios are expected to experience identical dynamics.

Each simulation is started from a fully developed turbulent flow at dimensionless time $t^+ = 0$ ($t^+ = t/t_v$) and is terminated at $t^+ \approx 29\,250$. Such a considerable long-time simulation is necessary to ensure that a statistically steady state for the particulate phase is attained, which is evidenced by the evolution of the Shannon entropy of particle distribution (see Appendix B for the details). The particles are released randomly in the entire computational domain at $t^+ = 0$. The initial velocity of each particle is set to be the fluid velocity at the particle position. The boundary conditions used in the present study are detailed in §§ 2.1–2.3 and illustrated by figure 1. For all statistics, the ensemble averaging, denoted by $\langle\cdot\rangle$, is performed over the horizontal directions and time hereafter. Here, 10 equally spaced snapshots in the time interval $t^+ \in [27\,300, 29\,250]$ are used for time averaging. The validation of our numerical simulation is presented in Appendix A.

3. Results and discussion

3.1. *Role of electrostatic forces in particle distribution*

To evaluate whether the electrostatic forces alter the particle distribution dramatically, we begin by comparing the instantaneous particle distributions of the uncharged and charged cases in various distinct wall-parallel planes, as displayed in figure 2. As reported previously, for the uncharged monodisperse case, the longitudinal particle streaks of length exceeding $10^3\delta_v$ exist in the viscous layer (figure 2*a*, left) (e.g. Ninto & Garcia 1996). Such streaks for the preferential concentration of particles become weaker in the buffer layer (figure 2*b*, left) and transition to cloud patterns in the outer layer (figure 2*c*, left). The formations of these clustering patterns are responsible for the fact that particles tend to aggregate into the low-speed velocity streaks in the near-wall region, but tend to collect in the high-speed regions in the outer layer (Marchioli & Soldati 2002; Sardina *et al.* 2012; Wang & Richter 2019). When particles are highly charged (i.e. $q = -0.01$ pC and

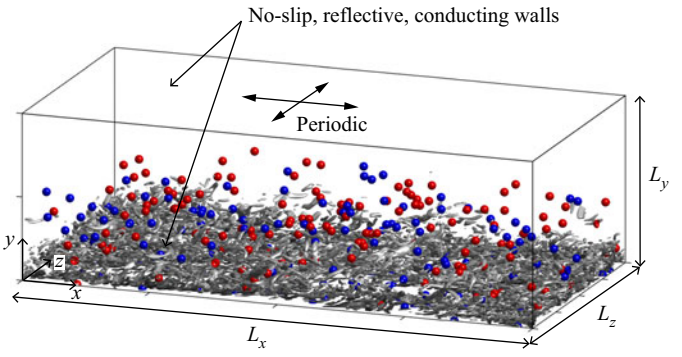

Figure 1. Sketch of the geometry and boundary conditions of the simulations. The periodic boundary conditions in the x- and z-directions are applied to the carrier fluid, particulate phase and electrical potential. The no-slip, reflective and conducting boundaries at the top and bottom walls are applied to the carrier fluid, particulate phase and electrical potential, respectively. The isosurfaces of the Q-criterion are shown at $Q = 150$ and are coloured by the streamwise velocity for the bidisperse case BD$^{\pm}$0.006 at $t^+ \approx 29\,250$. For clarity, only isosurfaces in the lower half of the channel are shown. Particles with wall distance $y < 0.2$ m are depicted in blue (red) for lighter (heavier) particles, where only every three thousand particles are shown.

$\overline{St_{el}} = 0.59 \times 10^{-2}$), the clustering patterns in different wall-parallel planes seem to be obscured to the bare eye, due to the considerable reductions in the particle concentrations (figures 2*a–c*, right). The quantitative measures are given further in § 3.3.

By contrast, the electrostatic effects in the bidisperse cases are somewhat different. For the uncharged lighter particles with $St^+ = 20$ (figures 2*d–f*, left), the same clustering patterns as in the uncharged monodisperse cases are observed as expected. However, the heavier particles with $St^+ = 400$ remain uniformly distributed (insets in figures 2*d–f*, left), owing to their very large inertia (i.e. see table 2, $St_{k,min} = 10.1$, which is much larger than unity). In contrast to the monodisperse cases, the number densities of the lighter and heavier particles are slightly changed by electrostatic forces, even in the presence of a large amount of electrical charge on particles (i.e. $q = \pm 0.1$ pC; figures 2*d–f*, right). Importantly, the lighter particles become much more uniformly distributed in the viscous layer when particles are highly charged, demonstrating that electrostatic forces indeed affect the distribution of the small-inertia particles.

To further assess the effects of electrostatic forces quantitatively, the wall-normal profiles of the mean particle number density are plotted in figure 3. All particle number densities are normalized by the bulk mean number density $n_0 = N/(L_x L_y L_z)$. In the case of flow laden with monodisperse uncharged particles, the mean particle number density decreases with increasing wall-normal location y^+ (figure 3*a*). This tendency of particle migration to the wall is caused by turbophoresis, as demonstrated in previous studies (Caporaloni *et al.* 1975; Reeks 1983; Marchioli *et al.* 2008). When the electrical charge on particles increases from 0 to -0.01 pC, the particle number density in the bulk of the channel is reduced considerably, especially at $y^+ \approx 1$, where it is decreased over two orders of magnitude. Meanwhile, the particle number density is increased substantially in a thin layer adjacent to the wall (i.e. $y^+ \sim 0.2$–0.3), suggesting that electrostatic forces enhance the particle wall accumulation in the monodisperse cases.

In the bidisperse cases, wall-normal distributions of the lighter and heavier particles exhibit quite different behaviours. When particles are not electrically charged (i.e. $q = 0$), the wall accumulation of the lighter particles is remarkable, while the heavier ones are rather uniformly distributed along the wall-normal direction (figure 3*b*). As electrical

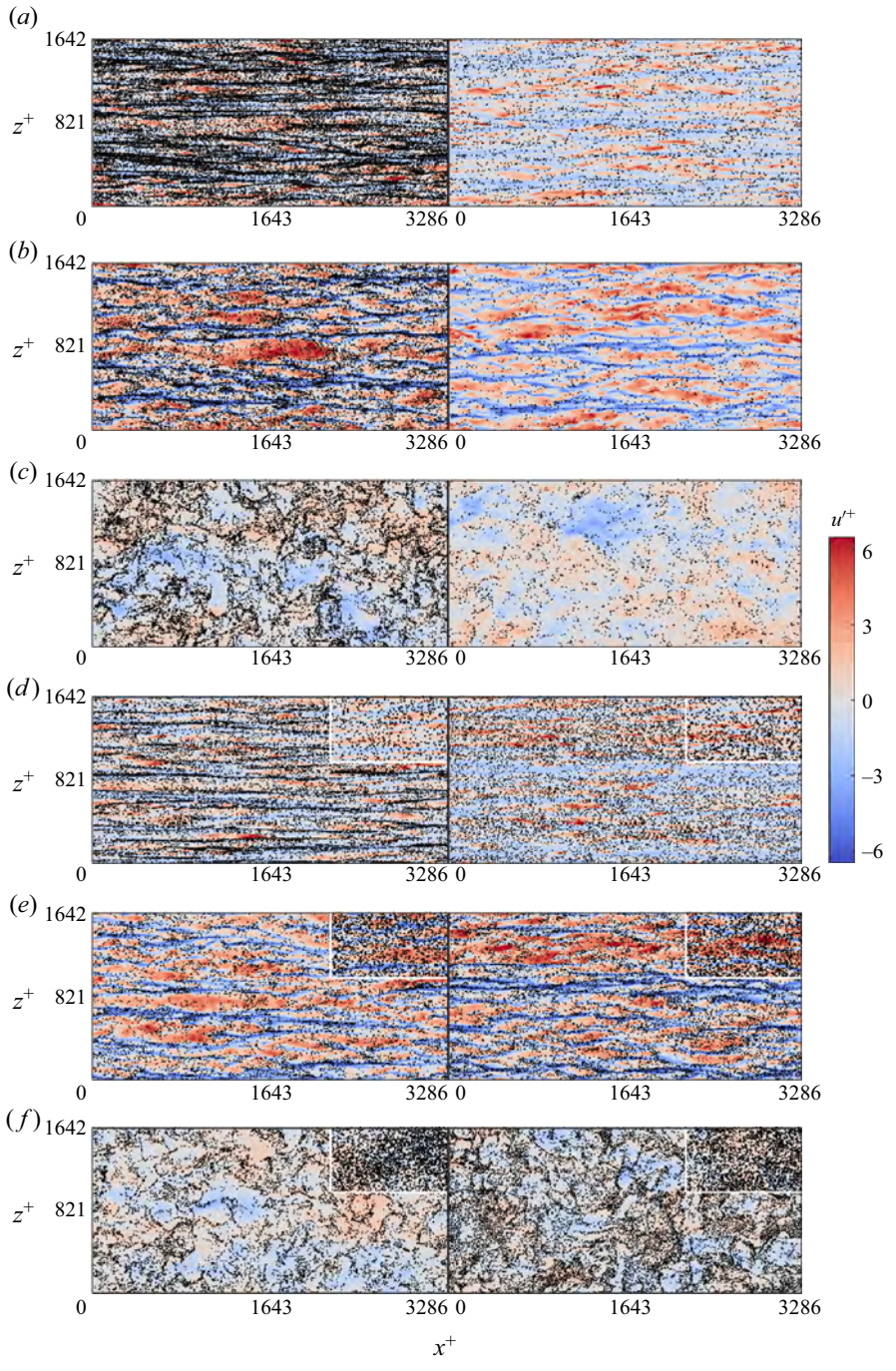

Figure 2. Instantaneous snapshots of the particle distribution in the wall-parallel (x–z) plane at $t^+ \approx 29\,250$ (not to scale). (a–c) Snapshots of the particle distributions in three layers $y^+ \in [2.1, 5.6]$, $[15.2, 25.0]$ and $[530.5, 548.5]$, respectively, and streamwise velocity fluctuations u'^+ at $y^+ = 3.8$, 20.5 and 539.5, for the monodisperse cases MD0 and MD0.01 ($St^+ = 20$). Here, the black dots depict the particles, and contours represent the fluctuating streamwise velocity. (d–f) Same as (a–c) but for bidisperse cases BD0 and BD$^{\pm}$0.1, where particles outside (inside) the white rectangles represent the lighter particles $St^+ = 20$ (heavier particles $St^+ = 400$). In each panel, the left-hand (right-hand) side represents the flow laden with uncharged (charged) particles.

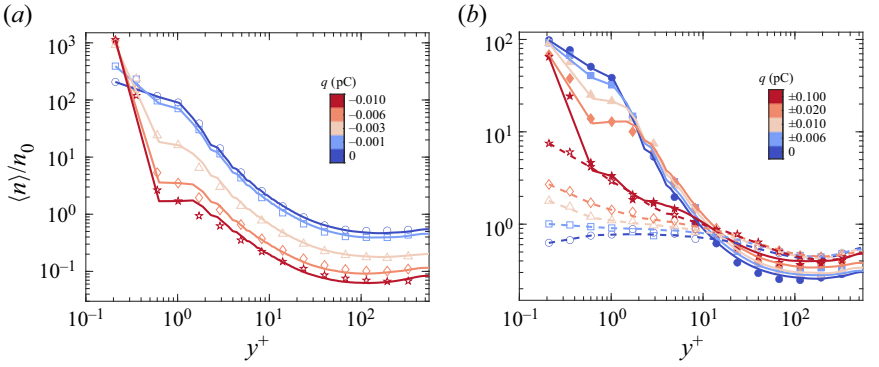

Figure 3. Wall-normal profiles of the mean particle number density for the (*a*) monodisperse ($St^+ = 20$) and (*b*) bidisperse ($St^+ = 20$ and $St^+ = 400$) cases. The mean particle number density $\langle n \rangle$ is normalized by the bulk mean number density n_0. The solid and dashed lines in (*b*) denote the lighter ($St^+ = 20$) and heavier ($St^+ = 400$) particles, respectively. The open and filled symbols denote the particle concentrations predicted by (3.1) for the lighter and heavier particles, respectively.

charge increases, the particle number density profile becomes flatter (steeper) for the lighter (heavier) particles. More specifically, the number density of the lighter particles is decreased in the wall layer but increased in the bulk of the channel (i.e. counter-clockwise pivoting effect). In contrast, there is an opposite effect for the heavier particles (i.e. clockwise pivoting effect). Consequently, the combined effect of the electrostatic forces tends to mitigate the concentration difference between the lighter and heavier particles.

The physical mechanisms for determining particle transport in the wall-normal direction can be deduced from the theoretical formulation of particle concentration:

$$n(y;t) = C \exp\left(\underbrace{\frac{1}{\tau_p}\int_0^y \frac{\langle \zeta\, v_{f@p} | \xi \rangle}{\langle v_p^2 | \xi \rangle}\,\mathrm{d}\xi}_{\textit{biased sampling}} + \underbrace{\frac{q}{m_p}\int_0^y \frac{\langle E_{y@p} | \xi \rangle}{\langle v_p^2 | \xi \rangle}\,\mathrm{d}\xi}_{\textit{electrostatic forces}} - \underbrace{\int_0^y \frac{\mathrm{d}\ln \langle v_p^2 | \xi \rangle}{\mathrm{d}\xi}\,\mathrm{d}\xi}_{\textit{turbophoresis}} \right), \tag{3.1}$$

which is derived from the kinetic equation for the single-point particle distribution function (Williams 1958; Sikovsky 2014; Johnson *et al.* 2020). Detailed information is offered in Appendix C. In (3.1), three phoresis integrals can be defined. The first term on the right-hand side accounts for the biased sampling of fluid velocity by particles, the second term represents the electrostatic drift, and the third term accounts for the turbophoresis. Therefore, the particle concentration profile is determined by the competition of turbophoresis, biased sampling and electrostatic drift, which is evidenced in figure 3 (symbols). Notably, (3.1) is obtained by neglecting the momentum exchanges between the lighter and heavier particles for the bidisperse cases. Qualitative agreement

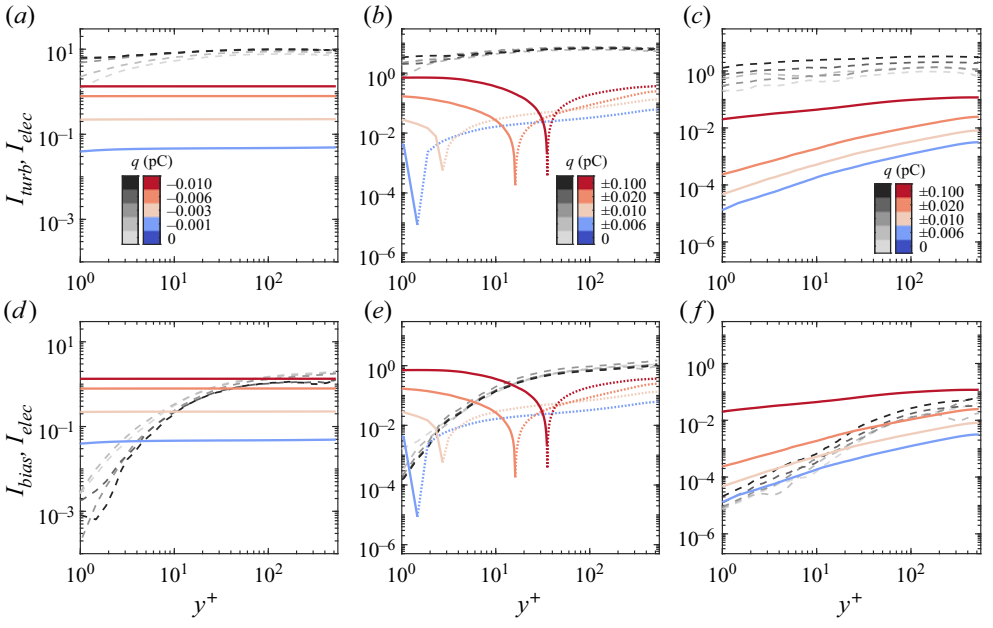

Figure 4. (*a–c*) Comparisons between turbophoresis integrals (I_{turb}, dashed lines) and electrostatic integrals (I_{elec}, solid lines). (*d–f*) Comparisons between biased sampling integrals (I_{bias}, dashed lines) and electrostatic integrals (I_{elec}, solid lines). Here, (*a*,*d*) correspond to the monodisperse cases, and (*b*,*e*) and (*c*,*f*) correspond to the lighter and heavier particles in the bidisperse cases, respectively. Note that the electrostatic integrals are shown by their absolute values for clarity, where the solid (dotted) lines representing their actual values are negative (positive).

of the theoretical predictions with simulation (figure 3*b*) indicates that these momentum exchanges are indeed negligible.

To explain why the wall-normal number density profiles of the monodisperse and bidisperse cases behave differently under the actions of electrostatic forces, the resulting three phoresis integrals are presented in figure 4. These integrals are computed numerically using a trapezoidal rule on a uniform grid with spacing $0.42\delta_v$. It is shown that for the monodisperse and bidisperse cases, the biased sampling and turbophoresis integrals are both positive and increase with increasing wall-normal location. This occurs because particles tend to accumulate in low-speed streaks of fluid flow (i.e. $\langle \zeta\, v_{f@p} | y \rangle > 0$) and there is a positive gradient of particle wall-normal velocity fluctuations (i.e. $\mathrm{d}\langle v_p^2 | y \rangle / \mathrm{d}y > 0$). According to (3.1), it is recognized that biased sampling leads to particles moving away from the wall, while turbophoresis results in a migration of particles towards the wall.

In monodisperse cases, electrostatic integrals are negative and nearly constant with the wall-normal location (figures 4*a*,*d*) because the mean wall-normal electric fields are directed towards the channel centreline and decrease sharply with increasing wall-normal location (not shown for brevity). Also, from (3.1), it is known that the wall-normal component of the electrostatic forces produces a drift of the particles to the wall and thus a considerable reduction of particle number density in the outer layer. This electrostatic drift is self-regulating, in which the particle number density in the outer layer declines until the wall-normal electric field is decreased to the point that an equilibrium transport is achieved. For the bidisperse cases, however, the electrostatic integrals of the lighter

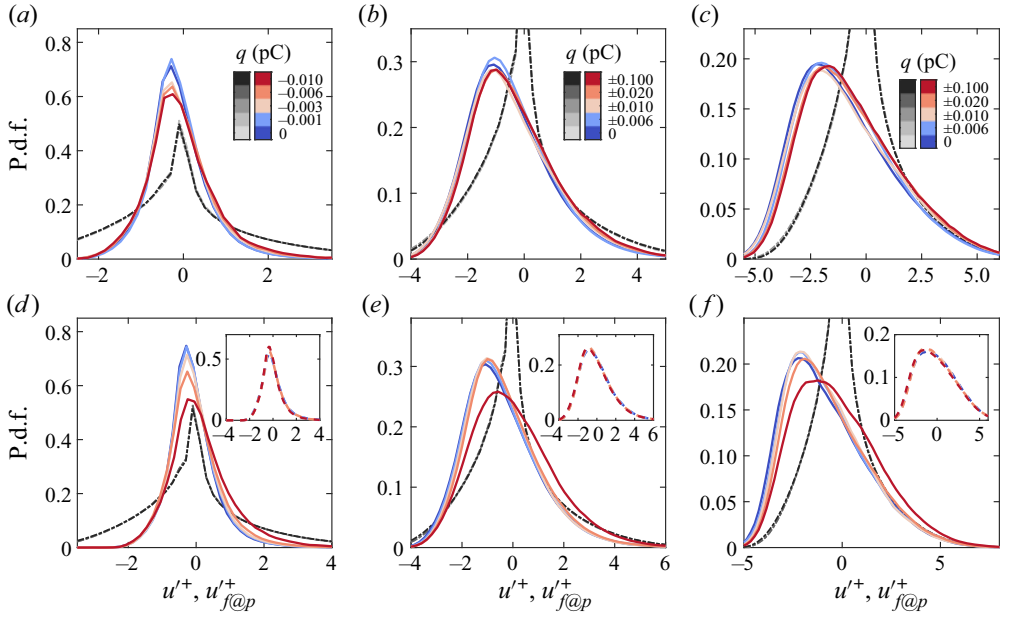

Figure 5. (*a–c*) In turn, the probability density functions (p.d.f.s) of the fluctuating streamwise fluid velocity at particle positions $u'^{+}_{f@p}$ (solid lines) in three wall layers $y^{+} \in [2, 4]$, $[4, 7]$ and $[7, 10]$, for the monodisperse cases ($St^{+} = 20$). (*d–f*) Same as (*a–c*) but for the bidisperse cases, where the dashed lines in the insets denote heavier particles ($St^{+} = 400$). For comparison, the fluctuating streamwise velocities u'^{+} (dash-dotted lines) are plotted.

particles are negative in a thin layer close to the wall, but positive above this layer (figures 4*b*,*e*), even though those of heavier particles are negative (figures 4*c*,*f*). As a result, electrostatic forces produce a wall-pointing drift very close to the wall but a channel-centreline-pointing drift in the bulk of the channel for the lighter particles. This bulk channel-centreline-pointing drift prevents particles moving towards the wall, leading to a reduction in the number density of lighter particles close to the wall, although the lighter particles tend to be held by electrostatic forces in a thin layer close to the wall. By contrast, heavier particles experience a wall-pointing electrostatic drift in the whole channel. Such different electrostatic effects for lighter and heavier particles very close to the wall are caused by their significant concentration differences in this layer. Overall, the wall-normal component of the electrostatic forces causes a particle to drift away from (towards) the wall for the lighter (heavier) particles. Doubtless, such a bidirectional electrostatic drift is responsible for the variations of particle number density profile in the wall-normal direction; the details will be discussed in § 3.2.

We end this subsection by clarifying how the positions of the particles correlate with the fluid velocity fields at various values of particle charge. First, we examine the probability density functions (p.d.f.s) of the fluctuating streamwise fluid velocity at particle positions (i.e. conditioned velocity $u'^{+}_{f@p}$) in the wall region, as shown in figure 5. It is clear that for the lighter particles in the uncharged monodisperse and bidisperse cases, the p.d.f.s of the conditioned velocity $u'^{+}_{f@p}$ deviate significantly from those of unconditioned fluctuating velocity u'^{+}. The p.d.f. peaks correspond to negative values of fluctuating streamwise fluid velocity, which verify quantitatively that lighter particles are trapped in the low-speed streaks of the fluid flow (Pedinotti *et al.* 1992; Marchioli & Soldati 2002).

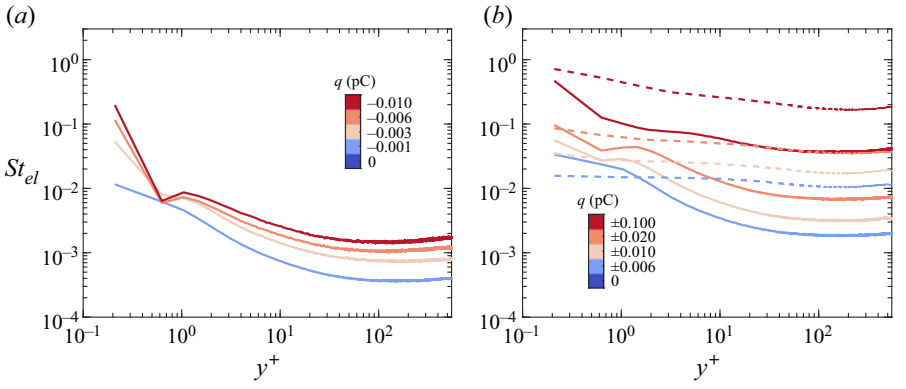

Figure 6. (*a*) Wall-normal profiles of the local particle electrostatic Stokes number St_{el} for the monodisperse cases. (*b*) Same as (*a*) but for the bidisperse cases, where the solid and dashed lines denote the lighter ($St^+ = 20$) and heavier ($St^+ = 400$) particles, respectively.

With increasing electrical charge, these p.d.f. peaks are slightly shifted towards zero and so suppress particle aggregation in the low-speed fluid streaks. The shifts in the buffer layer for the bidisperse cases are slightly larger compared to the monodisperse cases (e.g. figures 5*c*,*f*). The reason is that in the buffer layer, the local electrostatic Stokes numbers in the bidisperse cases are much larger than those in the monodisperse cases, as shown in figure 6. For the heavier particles in the bidisperse cases, the p.d.f.s of the conditioned and unconditioned velocities $u'^+_{f@p}$ and u'^+ are very similar, because the heavier particles are randomly distributed, and thus sample the fluid velocity fields uniformly. Also, the p.d.f. peaks are very close to zero and are unaffected by the electrostatic forces (insets in figures 5*d–f*). This is because electrostatic forces tend to homogenize the particle distribution in both monodisperse and bidisperse cases (as will be shown in § 3.3), so that does not alter the randomly distributed heavier particles. This result is in accordance with figures 2(*d*)–2(*f*).

In addition to the wall region, we use wall-normal profiles of the ratio between the particle numbers with $u'_{f@p} > 0$ and $u'_{f@p} < 0$ to quantify the distinct particle accumulations in the inner and outer layers, as done by Wang & Richter (2019). For the monodisperse cases, particle numbers of $u'_{f@p} < 0$ are larger (smaller) than those of $u'_{f@p} > 0$ in the inner (outer) layer, indicating that particles tend to collect in low-speed fluid streaks (high-speed regions) in the inner (outer) layer (figure 7*a*). This particle accumulation pattern is more weakened in the inner layer but more pronounced in the outer layer when increasing electrical charge. For the bidisperse cases, such a particle accumulation pattern still holds for the lighter and heavier particles but exhibits a different electrostatic effect (figure 7*b*). Specifically, the accumulation patterns of lighter particles in both inner and outer layers are inhibited by electrostatic forces, but the pattern of heavier particles remains nearly unchanged as mentioned above.

3.2. *Role of electrostatic forces in particle dynamics*

Having discussed the effects of electrostatic forces on particle distribution, we now turn our attention to how electrostatic forces affect particle dynamics. Figure 8 shows the wall-normal profiles of the mean particle streamwise velocity. The inertia of the lighter particles seems to be not substantial. The mean streamwise velocity of the lighter particles is smaller than the mean fluid streamwise velocity in the range $y^+ \in [5, 50]$, consistent

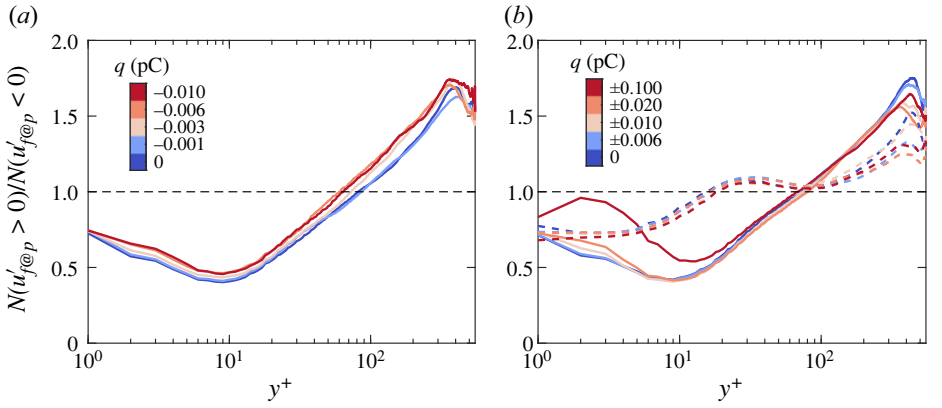

Figure 7. (*a*) Wall-normal profiles of the ratio between the particle number N with $u'_{f@p} > 0$ and $u'_{f@p} < 0$ for the monodisperse cases ($St^+ = 20$). (*b*) Same as (*a*) but for the bidisperse cases, where the solid and dashed lines denote the lighter ($St^+ = 20$) and heavier ($St^+ = 400$) particles, respectively.

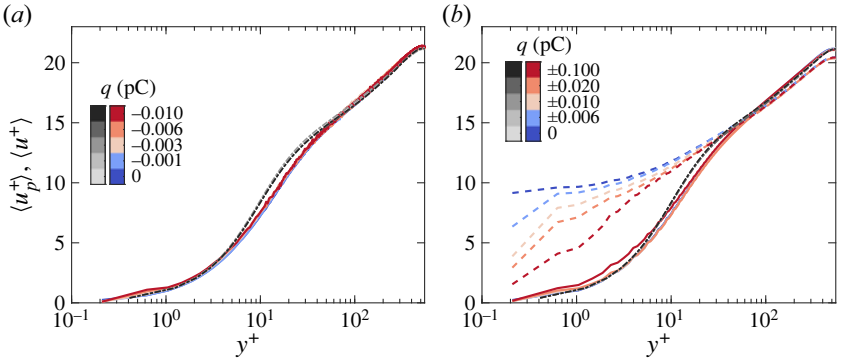

Figure 8. (*a*) Wall-normal profiles of the mean particle streamwise velocity $\langle u_p^+ \rangle$ (solid lines) for the monodisperse cases. (*b*) Same as (*a*) but for the bidisperse cases, where the solid and dashed lines denote the lighter ($St^+ = 20$) and heavier ($St^+ = 400$) particles, respectively. For comparison, the mean fluid streamwise velocity $\langle u^+ \rangle$ (dash-dotted line) is plotted.

with previous works (e.g. Arcen, Tanière & Oesterlé 2006). On the other hand, for the monodisperse and bidisperse cases, the mean streamwise velocities of the carrier fluid and the lighter particles are almost constant with electrical charges, suggesting a negligible electrostatic effect on them. This is because the St_{el} value of the lighter particles is of the order of $\sim O(10^{-3}$–$10^{-2})$ (figure 6), but the inter-particle electrostatic forces are found to be substantial only when the electrostatic Stokes number is at least of the order of $O(10^{-1})$ (Grosshans *et al.* 2021; Boutsikakis *et al.* 2022). Although St_{el} is up to $\sim O(10^{-1})$ at $y^+ \approx 0.2$ for the monodisperse cases (figure 6*a*), the electrostatic effect is also negligible because such a higher St_{el} region is too narrow ($\lesssim 0.1\delta_v$) and the corresponding mean particle streamwise velocity is very small ($\langle u_p^+ \rangle \sim 0.02$).

The behaviour of the heavier particles is rather different. First, when particles are uncharged, the heavier particles travel faster than the carrier fluid in the viscous and buffer layers (i.e. below $y^+ \approx 30$) but move slower than the carrier fluid above $y^+ \approx 30$. This can be explained by the fact that fast-moving heavier particles retain a fraction of their momentum when they are transported towards the wall and are not constrained

by the no-slip boundary condition (Kulick, Fessler & Eaton 1994; Li *et al.* 2012; Fong, Amili & Coletti 2019). Also, inter-particle collisions are thought to contribute to such larger-than-fluid mean particle streamwise velocity in the viscous and buffer layers, as pointed out by Vance, Squires & Simonin (2006) and Dritselis & Vlachos (2008). Second, and importantly, the mean streamwise velocity of the heavier particles is decreased considerably by electrostatic forces below $y^+ \approx 30$ (see figure 8*b*), because the electrostatic Stokes number is $St_{el} \gtrsim O(10^{-1})$ in this layer (see figure 6*b*), thus the effects of electrostatic forces on the motion of heavier particles become more pronounced. In particular, since particle number density decreases rapidly with increasing wall-normal location (figure 3), the St_{el} value in the outer layer is expected to be small (figure 6*b*), thereby leading to a negligible electrostatic effect above $y^+ \approx 30$.

Besides mean particle streamwise velocity, electrostatic forces alter the r.m.s. fluctuating velocity of the heavier particles significantly. The wall-normal profiles of the r.m.s. streamwise, wall-normal and spanwise particle fluctuating velocities for the monodisperse and bidisperse cases are presented in figure 9. The lighter particles display r.m.s. profiles similar to those of the carrier fluid. As expected, due to very low local electrostatic Stokes numbers above $y^+ \approx 10$, the electrostatic forces exhibit a negligible effect on all three components of the r.m.s. particle fluctuating velocity (figures 9*a–f*). In contrast, a slight change in the r.m.s. particle fluctuating velocities is observed below $y^+ \approx 10$, owing to the relatively larger electrostatic Stokes numbers. More importantly, the heavier particles display quite distinct r.m.s. velocity profiles compared with those of the carrier fluid (figures 9*g–i*), and experience much more intense velocity fluctuations throughout the channel. The r.m.s. fluctuating velocity of the heavier particles decreases with increasing electrical charge (corresponding to $\overline{St_{el}}$ ranging from 0 to ∼0.18), especially for the wall-normal and spanwise components, suggesting that electrostatic forces tend to suppress the turbulent fluctuations of the heavier particles.

Next, the skewness of the fluctuating velocity is shown in figure 10, which is a measure of the asymmetry of the p.d.f. of the fluctuating velocity. The negative (positive) skewness suggests that the p.d.f. is left-tailed (right-tailed), and a zero skewness suggests that the p.d.f. is symmetric. For the skewness of the spanwise velocity, both $S(w')$ and $S(w'_p)$ for the lighter and heavier particles are approximately zero above $y^+ \approx 15$ (figures 10*c*,*f*,*i*) in all simulated cases, indicating symmetric p.d.f.s of the spanwise velocities of the fluid and particulate phases (e.g. Pan & Banerjee 1997). For the skewness of the streamwise velocity, although $S(u'_p)$ deviates far from $S(u')$ for the heavier particles, they exhibit similar behaviours, which are positive close to the wall but negative away from the wall, with a zero value at approximately $y^+ \in [20, 30]$ (figures 10*a*,*d*,*g*), as reported previously by Wang *et al.* (2019). However, for the skewness of the wall-normal velocity, $S(v')$ and $S(v'_p)$ behave quite differently, especially for the bidisperse cases in which they are of opposite signs close to the wall (figures 10*b*,*e*,*h*). As the electrical charge increases, the variations of the streamwise and wall-normal skewness $S(u'_p)$ and $S(v'_p)$ appear to be slight for the monodisperse cases but become more noticeable for the bidisperse cases.

Combining the results of figures 9 and 10, it is known that particles' turbulent transport has been altered by electrostatic forces. In figure 11, we offer the wall-normal profiles of the particle Reynolds stress (i.e. the covariance of the particle streamwise and wall-normal velocities) in order to illustrate the underlying physical mechanisms. The trends in figure 11 are similar to those shown by the mean and r.m.s. of the particle velocity. Specifically, the Reynolds stress of the lighter particles is close to that of the carrier fluid throughout the channel, and increases (decrease) slightly with electrical charge below (above) $y^+ \approx 10$ (figures 11*a*,*b*). However, the Reynolds stress of the heavier particles deviates from that

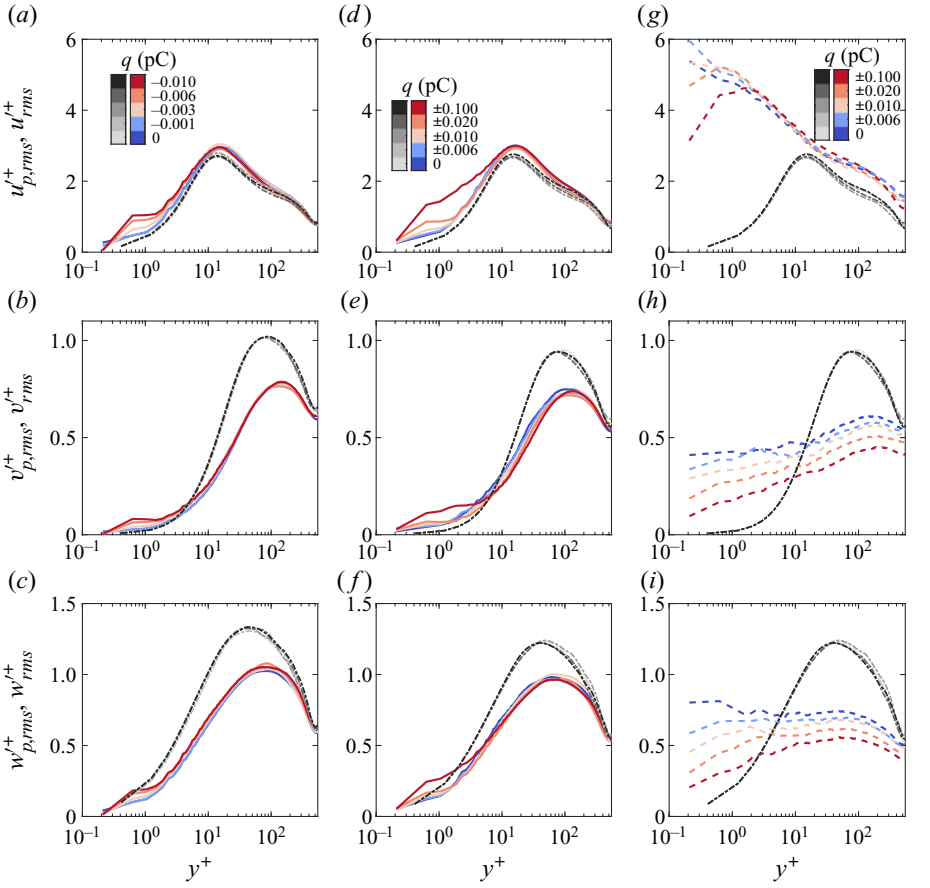

Figure 9. (*a–c*) In turn, the wall-normal profiles of the r.m.s. streamwise, wall-normal and spanwise particle fluctuating velocities ($u'^+_{p,rms}$, $v'^+_{p,rms}$ and $w'^+_{p,rms}$) for the monodisperse cases ($St^+ = 20$). (*d–f*) Same as (*a–c*) but for the lighter particles ($St^+ = 20$) in the bidisperse cases. (*g–i*) Same as (*a–c*) but for the heavier particles ($St^+ = 400$, dashed lines) in the bidisperse cases. For comparison, the r.m.s. streamwise, wall-normal and spanwise fluid fluctuating velocities (u'^+_{rms}, v'^+_{rms} and w'^+_{rms}, dash-dotted lines) are plotted.

of the carrier fluid in the inner layer (below $y^+ \approx 150$) and is significantly reduced when experiencing electrostatic forces (figure 11*b*).

To assess the dynamics further, we perform a quadrant analysis for the fluid and particle Reynolds stresses in the u'^+–v'^+ and u'^+_p–u'^+_p planes, providing detailed information on the contribution to turbulence production from various events (see figure 12). The Reynolds stress is classified into four quadrants (i.e. Q1–Q4) based on the signs of the fluctuating velocities. For example, regarding the particle Reynolds stress, we have $u'^+_p > 0$ and $v'^+_p > 0$ for Q1, $u'^+_p < 0$ and $v'^+_p > 0$ for Q2, $u'^+_p < 0$ and $v'^+_p < 0$ for Q3, and $u'^+_p > 0$ and $v'^+_p < 0$ for Q4. The Q2 and Q4 events are associated with low-speed ejections and high-speed sweeps, respectively (Wallace, Eckelmann & Brodkey 1972; Li *et al.* 2012). As shown in figure 12, for both fluid and particulate phases in all simulated cases, Q2 and Q4 events dominate and contribute to the positive Reynolds shear stress $-\langle u'^+_p v'^+_p \rangle$ and $-\langle u'^+ v'^+ \rangle$. Meanwhile, the Q1–Q4 events of the lighter particles behave similarly to those of the fluid phase (figures 12*a–h*), indicating that sweep

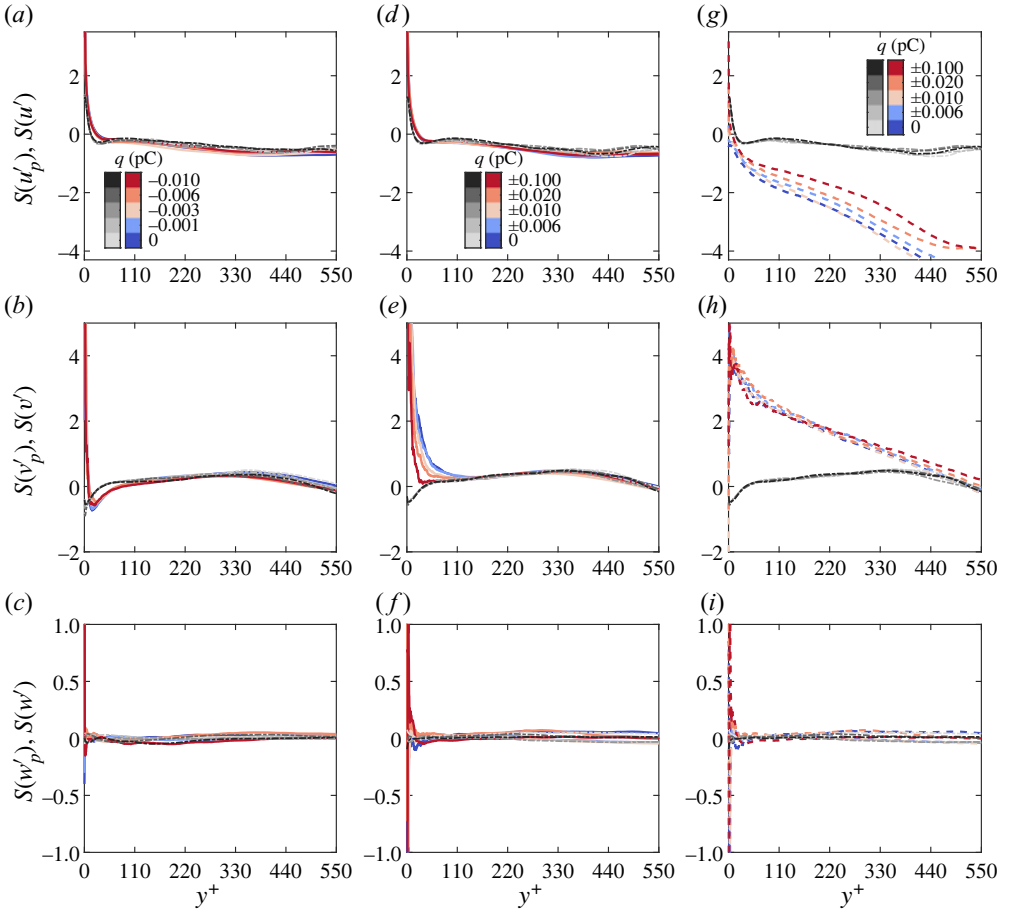

Figure 10. (*a–c*) In turn, the wall-normal profiles of the skewness of streamwise, wall-normal and spanwise particle fluctuating velocities ($S(u'_p)$, $S(v'_p)$ and $S(w'_p)$) for the monodisperse cases ($St^+ = 20$). (*d–f*) Same as (*a–c*) but for the lighter particles ($St^+ = 20$) in the bidisperse cases. (*g–i*) Same as (*a–c*) but for the heavier particles ($St^+ = 400$, dashed lines) in the bidisperse cases. For comparison, the skewness of the streamwise, wall-normal and spanwise fluid fluctuating velocities ($S(u')$, $S(v')$ and $S(w')$, dash-dotted lines) is plotted.

and ejection events are crucial in particle transfer (e.g. Fong *et al.* 2019). Importantly, these events are approximately constant with electrostatic forces, which is consistent with electrostatics-invariant turbophoresis and biased sampling integrals in figure 4. This means that electrostatic forces alter the transport of lighter particles only through electrostatic drifts, while keeping the turbophoresis and biased sampling effects unchanged. By contrast, the Q1–Q4 events of the heavier particles deviate far from those of the fluid phase, and their magnitudes are affected by electrostatic forces apparently (figures 12*i–l*), suggesting that electrostatic forces have a pronounced effect on heavier particle turbulent transport. It is worthwhile to note that when heavier particles are uncharged, the particle's Q2 and Q4 events are approximately equal in magnitude below $y^+ \approx 10$, thus heavier particles transfer equally to the wall and away from the wall, indicating a relatively shallow profile of the particle number density (see figure 3*b*). However, when heavier particles are highly charged, the particle Q4 events become much more pronounced than particle Q2 events below $y^+ \approx 10$ (figures 12*j*,*l*), causing heavier particles to be swept towards the

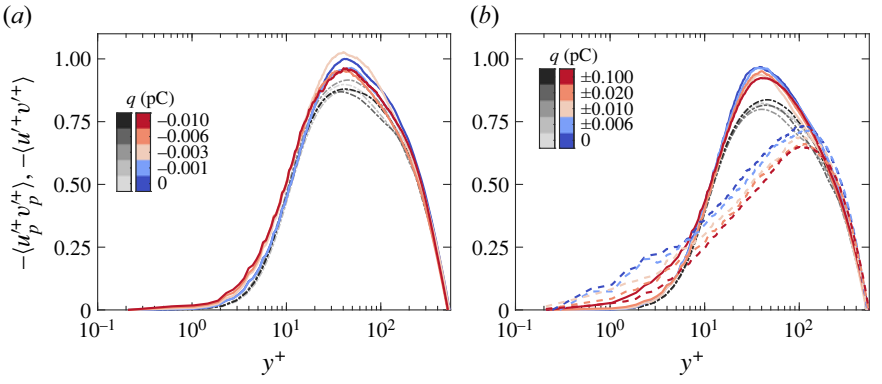

Figure 11. (*a*) Wall-normal profiles of the particle Reynolds stress $-\langle u_p'^{+} v_p'^{+} \rangle$ (solid lines) for the monodisperse cases. (*b*) Same as (*a*) but for the bidisperse cases, where the solid and dashed lines denote the lighter ($St^{+} = 20$) and heavier ($St^{+} = 400$) particles, respectively. For comparison, the fluid Reynolds stress $-\langle u'^{+} v'^{+} \rangle$ (dashed lines) is plotted.

wall and accumulated in the wall region (figure 3*b*). This phenomenon corresponds to the significant enhancements of turbophoresis integrals in figure 4(*c*), which is attributed to the remarkable reduction in wall-normal particle r.m.s. velocity fluctuations (figure 9*h*). In such a case, the increases of electrostatic integrals are much smaller than those of turbophoresis integrals (see figure 4*c*) so that the wall-normal transports of heavier particles towards the wall are indirectly strengthened by the enhanced turbophoresis. In other words, we conclude that there are two distinct mechanisms responsible for the modulation of the transport of lighter and heavier particles by electrostatic forces. The wall-normal transport of lighter particles is modulated directly by electrostatic drift, whereas that of heavier particles is altered indirectly by strengthening turbophoresis.

3.3. *Role of electrostatic forces in particle clustering*

To elucidate how the electrostatic forces affect particle clustering, finally we use two-dimensional Voronoï analysis and angular distribution functions of particles in the wall-parallel planes to quantify the degree and spatial pattern of particle accumulation. Figure 13 shows an example of the Voronoï analysis of particles residing in a thin layer $y^{+} \in [4, 6]$. It is clear that large-scale particle streaks of streamwise length exceeding $10^{3}\delta_{\nu}$ prevail in the wall region (figure 13*a*). In Voronoï analysis, the wall-parallel plane has been decomposed into a finite number of Voronoï cells according to the particle's position (figure 13*b*), where each cell contains the set of points closer to that particle than to any other (e.g. Aurenhammer 1991). The area of a Voronoï cell is inversely proportional to local particle concentration, and therefore can be regarded as a convenient measure of the degree of the particle clustering (Monchaux, Bourgoin & Cartellier 2010; Tagawa *et al.* 2012; Uhlmann & Doychev 2014; Petersen, Baker & Coletti 2019; Liu *et al.* 2020; Zhu *et al.* 2021; Apte *et al.* 2022).

To evaluate quantitatively the effects of electrostatic forces on the degree of particle clustering, the p.d.f.s of the Voronoï areas in three distinct layers (viscous, buffer and channel centreline) are presented in figure 14, where the Voronoï area A is normalized by its mean value $\langle A \rangle$. For comparison, the p.d.f. of the normalized Voronoï areas of the randomly distributed particles with the same particle number density is shown, which is well described by a Γ distribution (Ferenc & Néda 2007). Clearly, there are two

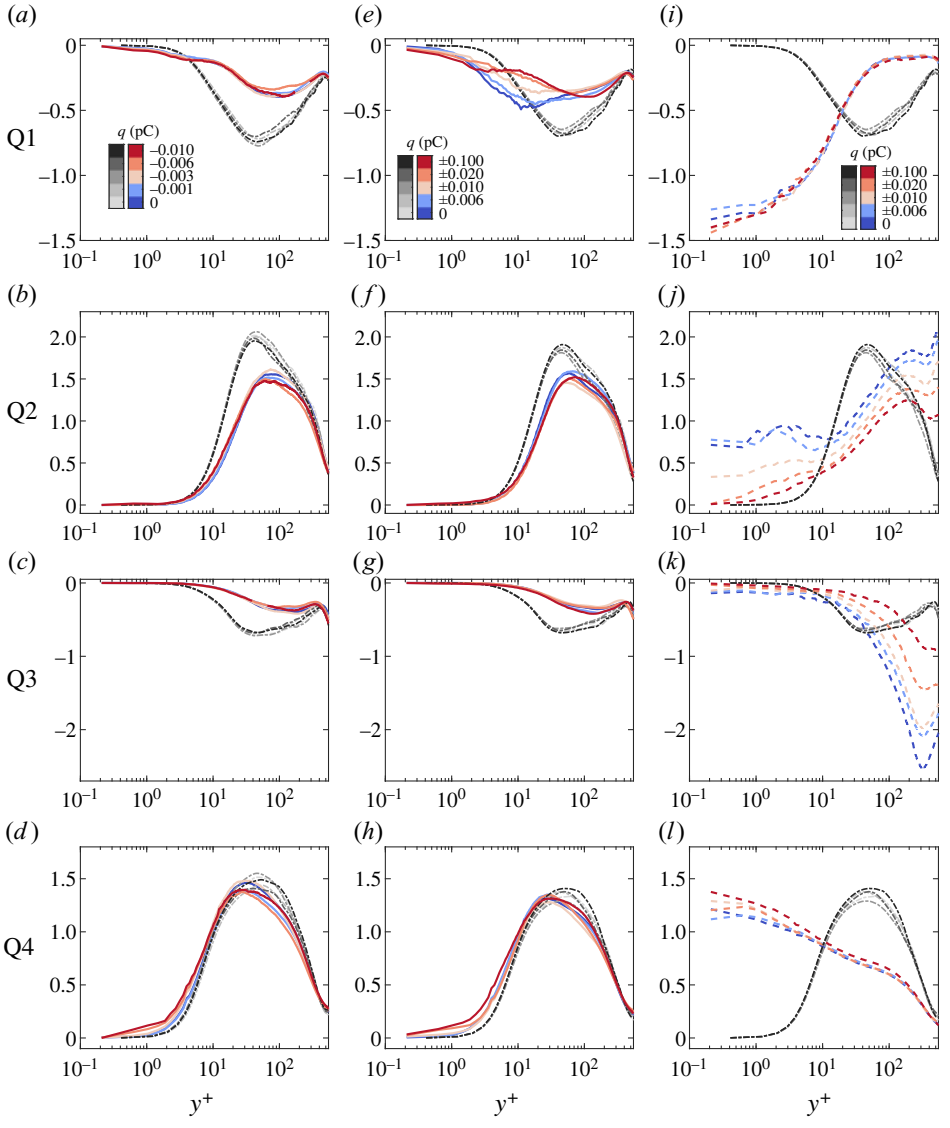

Figure 12. (*a–d*) In turn, the contributions of Q1 to Q4 quadrants of the u'^{+}_{p}–v'^{+}_{p} plane to the particle Reynolds stress $-\langle u'^{+}_{p} v'^{+}_{p}\rangle$ (solid lines) for the monodisperse cases. (*e–h*) Same as (*a–d*) but corresponding to the lighter ($St^{+} = 20$) particles for the bidisperse cases. (*i–l*) Same as (*a–d*) but corresponding to the heavier ($St^{+} = 400$) particles for the bidisperse cases. For comparison, the contributions of Q1 to Q4 quadrants to the fluid Reynolds stress $-\langle u'^{+} v'^{+}\rangle$ (dash-dotted lines) are plotted.

intersection points between the p.d.f.s of the preferentially (solid lines) and randomly (dashed lines) distributed particles, which appear to not evolve with increasing particle's electrical charge and wall-normal location. The Voronoï cell having an area smaller than the first intersection point (i.e. $A/\langle A\rangle \approx 0.4$) can be identified as a cluster, while the Voronoï cell is considered as a void if its area is larger than the second intersection point (i.e. $A/\langle A\rangle \approx 2.5$) (e.g. Monchaux, Bourgoin & Cartellier 2012). For the lighter particles in all simulated cases, the p.d.f.s in three distinct layers are much wider and highly left-skewed compared to the random Γ distribution, suggesting that lighter particles

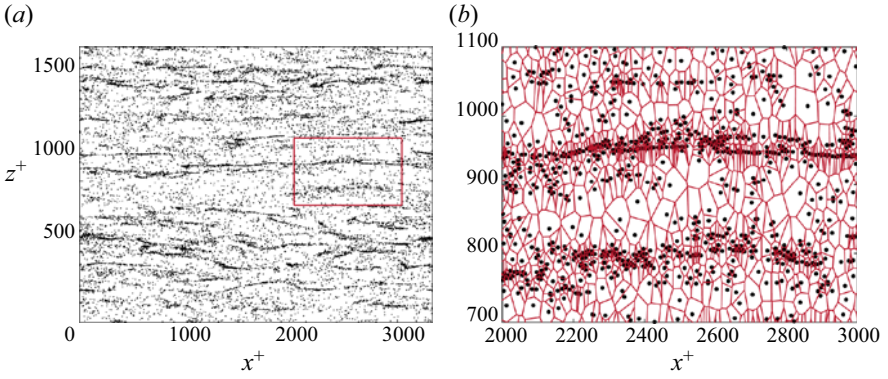

Figure 13. (*a*) Instantaneous snapshot of particle distribution in the layer $y^+ \in [4, 6]$ at $t^+ = 29\,250$ for the monodisperse case MD0 ($St^+ = 20$). (*b*) A magnified view with Voronoï tessellation corresponding to the red rectangle in (*a*).

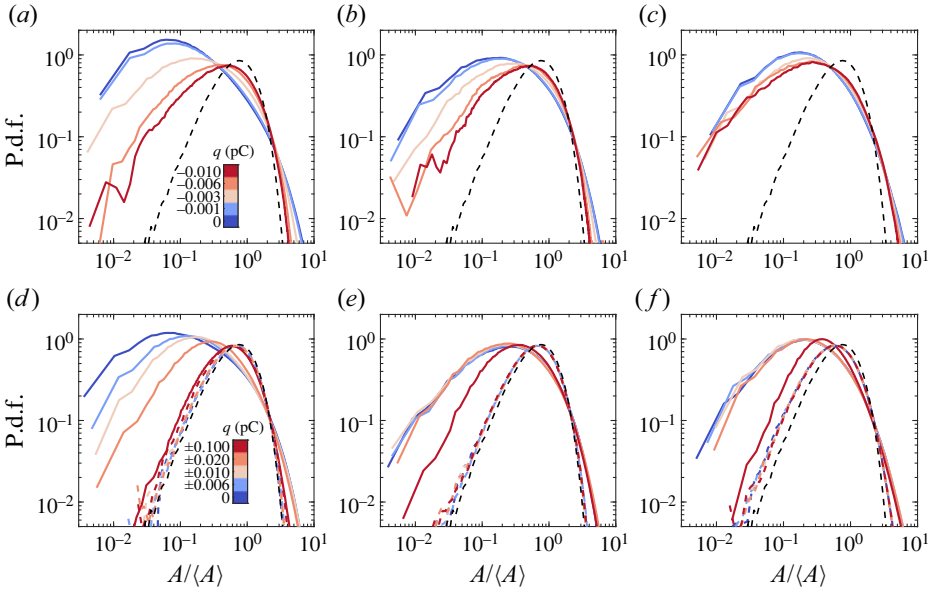

Figure 14. (*a–c*) In turn, the p.d.f.s of the normalized Voronoï areas $A/\langle A\rangle$ in three layers, $y^+ \in [2.1, 5.6]$, $[15.2, 25.0]$ and $[530.5, 548.5]$, for the monodisperse cases ($St^+ = 20$). (*d–f*) Same as (*a–c*) but for the bidisperse cases, where the coloured solid and dashed lines represent the lighter ($St^+ = 20$) and heavier ($St^+ = 400$) particles, respectively. The black dashed lines represent the p.d.f.s for the randomly distributed particles, which can be approximately by a Γ distribution.

concentrate preferentially. In addition, for the monodisperse cases, the peak and extent of the p.d.f.s at the channel centreline are significantly smaller than those in the wall region (figures 14*a–c*), indicating weaker clustering. However, the p.d.f.s seem to be not significantly changed with the wall-normal location for the bidisperse cases.

Importantly, the effects of electrostatic forces on the p.d.f.s of lighter particles are prominent. As electrical charge increases, the p.d.f.s of the lighter particles in both monodisperse and bidisperse cases become progressively close to the random Γ distribution, suggesting that electrostatic forces have a tendency to destroy

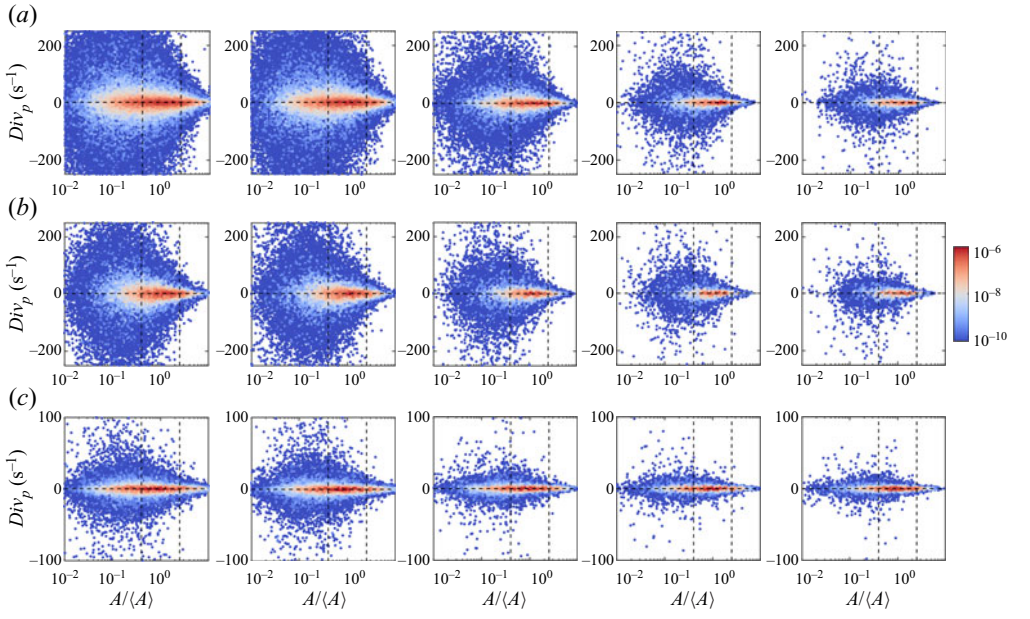

Figure 15. (*a*) Joint p.d.f.s of the divergence of the particle velocity Div_p and the area of the Voronoï cells $A/\langle A\rangle$/ for the monodisperse cases in the layer $y^+ \in [2.1, 5.6]$. Left-to-right: the electrical charge of particles varies from 0 to −0.01 pC. (*b*,*c*) Same as (*a*) but for the particles in the layers $y^+ \in [15.2, 25.0]$ and [530.5, 548.5], respectively. In each plot, the first and second vertical dashed lines correspond to $A/\langle A\rangle = 0.4$ and 2.5, respectively.

particle clustering. Interestingly, even though electrostatic forces considerably alter the concentration and dynamics of the heavier particles in bidisperse cases, they do not play a important role in the formation or destruction of clustering, as shown in figures 14(*d–f*). This might be explained by assuming that electrostatic forces also tend to homogenize heavier particles.

To further reveal how the electrostatic forces affect the clustering dynamics, we present the joint p.d.f.s of the divergence of the particle velocity Div_p and the Voronoï area $A/\langle A\rangle$ in figures 15 and 16. The divergence Div_p is evaluated by the Voronoï-based method proposed by Oujia, Matsuda & Schneider (2020), which gives

$$Div_p = \frac{2}{\Delta t}\frac{A^{k+1} - A^k}{A^{k+1} + A^k} + O(\Delta t), \tag{3.2}$$

with first-order approximation. Here, A^k and A^{k+1} denote the Voronoï areas at time instants t^k and $t^{k+1} = t^k + \Delta t$. The time step Δt is set to be 5×10^{-4}, which is chosen sufficiently small. Typically, a larger (smaller) area $A/\langle A\rangle$ with negative divergence Div_p represents clustering formation (strengthening), whereas a smaller (larger) area $A/\langle A\rangle$ with positive divergence Div_p represents void formation (strengthening).

In figures 15 and 16, the joint p.d.f.s for the lighter particles in all cases are almost symmetric with respect to the line $Div_p = 0$, suggesting a statistically dynamic equilibrium of formation and destruction of clusterings and voids. As electrical charge increases, the peaks of the joint p.d.f.s in the viscous and buffer layers tend to shrink into the region between the two vertical dashed lines (figures 15*a* and 16*a*), suggesting that the majority of clusterings and voids are considerably destroyed by electrostatic forces and become more uniformly distributed. In the channel centreline, the variations of the joint p.d.f.s

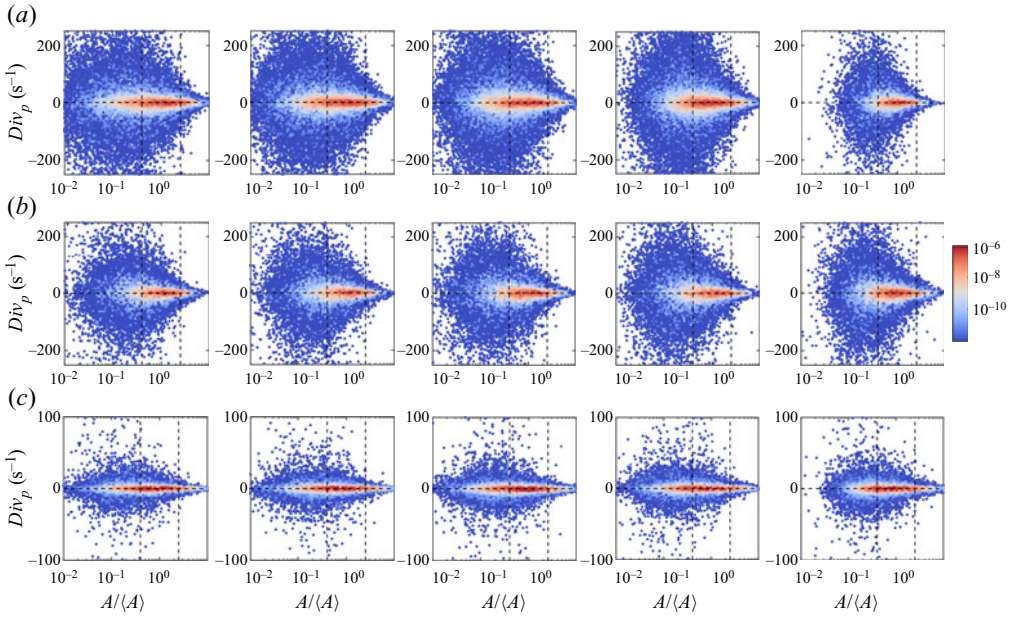

Figure 16. (*a*) Joint p.d.f.s of the divergence of the particle velocity Div_p and the area of the Voronoï cells $A/\langle A\rangle/$ for the lighter particles in the bidisperse cases within the layer $y^+ \in [2.1, 5.6]$. Left-to-right: the electrical charge of particles varies from 0 to -0.1 pC. (*b*,*c*) Same as (*a*) but for the particles in the layers $y^+ \in [15.2, 25.0]$ and $[530.5, 548.5]$, respectively. In each plot, the first and second vertical dashed lines correspond to $A/\langle A\rangle = 0.4$ and 2.5, respectively.

with electrical charge appear to be relatively mild, especially for the bidisperse case (figures 16*c*). In this case, the near-Γ distribution of the Voronoï areas at large electrical charge (i.e. figure 14*f*) is believed to be attributed to the increase in particle number density rather than altering clustering dynamics (Tagawa *et al.* 2012). Additionally, the joint p.d.f.s of the heavier particles in the bidisperse cases (not shown for brevity) are found to be constant with electrical charge, whose peaks are bounded within $A/\langle A\rangle \in [0.4, 2.5]$, in agreement with the uniform distributions of heavier particles.

After assessing the degree of particle accumulation and clustering dynamics, we then use angular distribution functions (ADFs) of particles (e.g. see Fong *et al.* 2019; Wang *et al.* 2019) to quantify the spatial pattern of clustering in the wall-parallel planes, which is defined by

$$\mathrm{ADF} = \frac{\langle \delta N_i(r,\theta)/(\delta r\, \delta\theta)\rangle}{N/(L_x L_z)}, \tag{3.3}$$

where $\delta N_i(r,\theta)$ is the number of particles located in a sector within $[r, r+\delta r]$ in the radial direction and $[\theta, \theta+\delta\theta]$ in the angular direction from the centre of particle i. Here, N is the total number of particles within the considered slab, and the average is taken over all particles in this slab. Also, $\theta = 0^\circ$ and $\theta = 90^\circ$ correspond to the spanwise and streamwise directions, respectively. For particles near the boundaries in the streamwise and spanwise directions, periodic boundary conditions are used. In principle, such ADFs characterize the statistically averaged accumulation structures of the particle clustering in the wall-parallel planes, providing a measure of the anisotropy of particle clustering in both distance and direction. Note that besides the ADFs, two-dimensional autocorrelation functions of particle number density are also used to extract the average

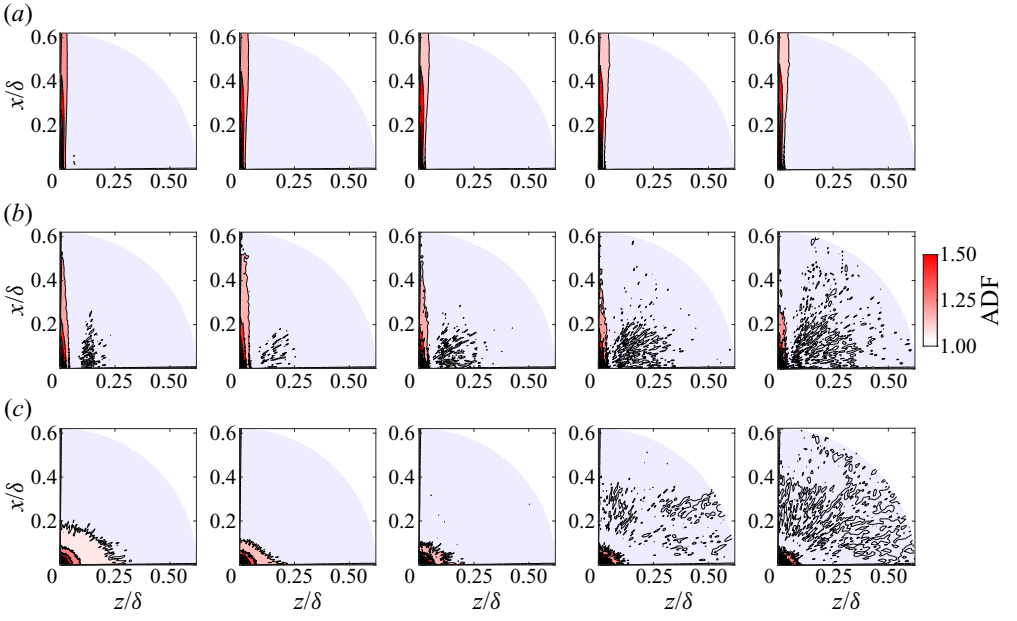

Figure 17. (*a*) ADFs of particles in the layer $y^+ \in [2.1, 5.6]$ for the monodisperse cases. Left-to-right: the electrical charge of particles varies from 0 to −0.01 pC. (*b*,*c*) Same as (*a*) but for the particles in the layers $y^+ \in [15.2, 25.0]$ and [530.5, 548.5], respectively.

clustering structure (e.g. Sardina *et al.* 2011; Jie *et al.* 2022), but they are difficult to converge numerically at very low particle concentrations.

The ADFs of the lighter particles for the monodisperse and bidisperse cases are shown in figures 17 and 18, respectively. It can be seen that the clustering structure is highly streamwise-elongated in the viscous and buffer layers, and remains nearly unchanged with electrical charge (figures 17*a*,*b* and 18*a*,*b*). This means that although particles are more uniformly distributed at large electrical charge, the anisotropy of particle clustering still holds in near-wall region, consistent with the instantaneous distribution (e.g. figures 2*a*,*b* and 2*d*,*e*, right). This occurs because electrostatic forces tend to homogenize particles in the spanwise direction, while the velocity fluctuations still dominate the streamwise layout of the particles. Such an anisotropic streaky structure disappears and becomes nearly isotropic at the channel centreline, i.e. contour lines of ADFs being circles (figures 17*c* and 18*c*). The reason is that the distribution of lighter particles is closely related to the fluid velocity field, which is streaky in the wall region and tends to be more isotropic at the channel centreline. In particular, the spatial extent of this isotropic ADF is progressively decreased (increased) with increasing electrical charge by a factor of two in the monodisperse (bidisperse) cases, which can also be observed qualitatively in figures 2(*c*) and 2(*f*). As discussed previously, the inhibited (enhanced) ADFs are due mainly to the reduction (increase) of particle concentration at the channel centreline because the clustering dynamics are invariant with electrical charge in this region. By contrast, since the heavier particles are randomly distributed, their ADFs for all simulated cases do not display any well-defined patterns (not shown for brevity).

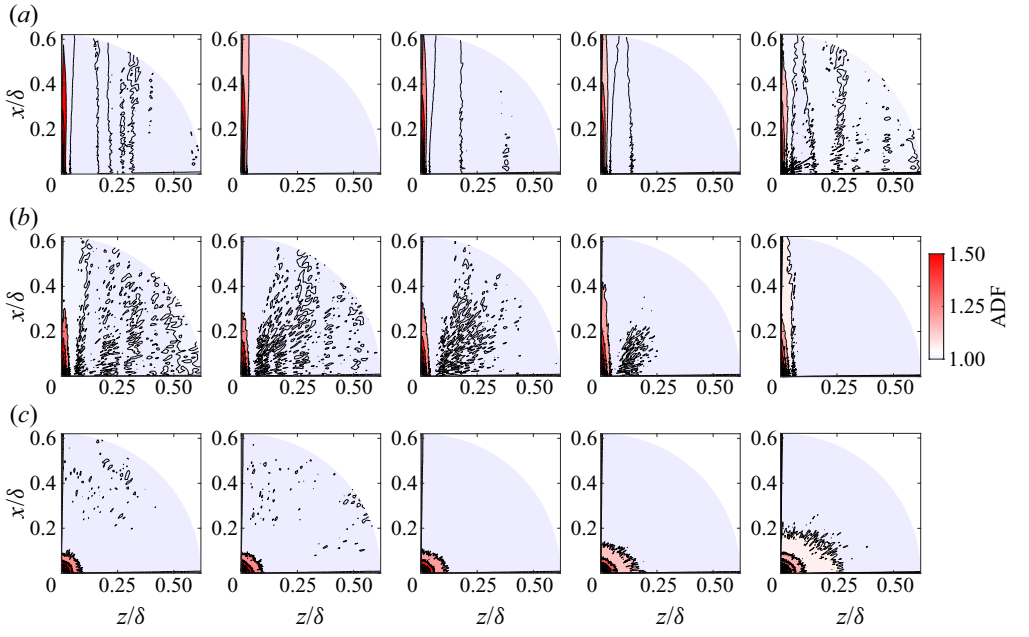

Figure 18. (*a*) ADFs of the lighter particles in the layer $y^+ \in [2.1, 5.6]$ for the bidisperse cases. Left-to-right: the electrical charge of particles varies from 0 to −0.1 pC. (*b*,*c*) Same as (*a*) but for the lighter particles in the layers $y^+ \in [15.2, 25.0]$ and [530.5, 548.5], respectively.

4. Conclusions

To elucidate the roles of electrostatic forces in particle behaviour in wall-bounded turbulent flows, we have performed DNS of turbulent channel flows at friction Reynolds number $Re_\tau = 550$ laden with two particulate systems: like-charged monodisperse and oppositely charged bidisperse particles. The simulations were conducted using a coupled Eulerian–Lagrangian point-particle approach, in which the particle–turbulence and particle–electrostatics two-way couplings, as well as inter-particle collisions, are taken into account because of the locally very high particle number density and mass loading caused by preferential concentration and turbophoresis. In monodisperse cases, the particles are identically charged and their viscous Stokes number is set to be $St^+ = 20$. In bidisperse cases, the lighter and heavier particles are negatively and positively charged, respectively, where the viscous Stokes number for the former is $St^+ = 20$ and for the latter is $St^+ = 400$.

From the DNS data, we find that the particle–electrostatics interaction becomes more prominent when the local electrostatic Stokes number reaches $St_{el} \sim O(10^{-1})$, and exhibits somewhat different features in the monodisperse and bidisperse cases. The particle accumulation in a thin layer adjacent to the wall is enhanced considerably by electrostatic forces in the monodisperse cases, because particle electrostatic drift is directed towards the wall. Overall, the lighter and heavier particles are oppositely drifted along the wall-normal direction by electrostatic forces, thereby leading to mitigation of their significant concentration differences. These electrostatic drifts are self-regulating for maintaining the particle transport at equilibrium. Also, preferential distribution of lighter particles in the low-speed fluid streaks (high-speed fluid regions) in the inner (outer) layers

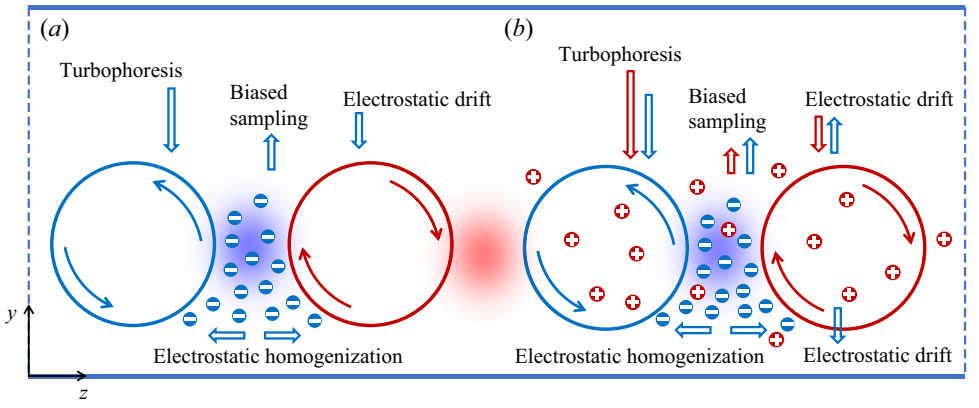

Figure 19. Schematic diagram of the main particle transport processes in the (*a*) monodisperse and (*b*) bidisperse cases.

is altered by electrostatic forces, besides remaining unchanged for the heavier particles in the bidisperse cases.

Although electrostatic forces slightly alter the dynamics of lighter particles, they modulate that of heavier particles remarkably because of their relatively strong particle–electrostatics interactions. In particular, the mean streamwise velocity of the heavier particles decreases with increasing electrical charge below $y^+ \approx 30$, but remains approximately constant above this wall-normal location. The r.m.s. fluctuating velocities of the heavier particles deviate from those of carrier fluid and are also suppressed by electrostatic forces throughout the channel. A particle's ejection and sweep events are approximately constant with (significantly altered by) electrostatic forces for the lighter (heavier) particles. This suggest that there exist two distinct mechanisms responsible for the modulation of the transport of lighter and heavier particles. The wall-normal transport of lighter particles is modulated directly by electrostatic drift, while that of heavier particles is altered indirectly by strengthening turbophoresis.

Furthermore, in both monodisperse and bidisperse cases, the clustering degree of the lighter particles is found to decrease with increasing electrical charge, suggesting that electrostatic forces tend to homogenize particle distribution in the wall-parallel planes. Importantly, the anisotropic streaky clustering in the wall region still holds at large electrical charge level. At the channel centreline, however, the size of the clustering is significantly reduced (increased) by electrostatic forces.

A schematic view summarizing the main physical processes affecting particle behaviour is presented in figure 19. For the monodisperse cases, there are four main physical processes affecting particle behaviour (figure 19*a*): (i) turbophoresis drift from the outer layer to the wall caused by non-uniform distribution of turbulent intensity; (ii) biased sampling of fluid flow by particles, leading to particles moving away from the wall; (iii) electrostatic drift caused by the electric field in the wall-normal direction, causing a migration of particles towards the wall; and (iv) the electrostatic homogenization of particles in the spanwise direction very close to the wall, inhibiting the formation and destruction of particle clusterings and voids. For the particle transport in the wall-normal direction, turbophoresis effects are the most prominent, with biased sampling and electrostatic drift being of secondary importance. As indicated in figure 19(*b*), the electrostatic effects in the bidisperse cases are quite different from those in the

monodisperse cases, even though the turbophoresis and biased sampling effects are very similar. Specifically, the electrostatic drift of the lighter particles is directed away from the wall in the bulk of the channel, but towards the wall in a thin layer close to the wall. Such a near-wall electrostatic drift is due to large concentration differences between the lighter and heavier particles in this layer. On the other hand, except for no significant electrostatic homogenization due to inherent uniform distribution, heavier particles experience similar turbophoresis and electrostatic drift but a relatively weaker biased sampling in the wall-normal direction.

In this work, several important issues have not been considered and deserve further investigation. For example, turbulence is expected to be modulated indirectly by electrostatic forces at high particle mass loading because in this case particle behaviour is altered dramatically by electrostatic forces, but the detailed modulation is unclear. As mentioned in the Introduction, particle clustering is multi-scale in high-Reynolds-number flows, but the effects of electrostatic forces on such multi-scale clustering remain unknown. These two cases are a common occurrence in industrial and natural conditions. Additionally, the monodisperse cases comprising two groups of particles with opposite electrical charge, and bidisperse cases comprising particles with identical electrical charge, are of great importance in practical applications. These cases are explored briefly in Appendix D.

Funding. This work was supported by the National Natural Science Foundation of China (grant no. 92052202), the National Numerical Windtunnel project, and the Fundamental Research Funds for the Central Universities (grant no. lzujbky-2021-ey19).

Declaration of interests. The authors report no conflict of interests.

Author ORCIDs.
Huan Zhang https://orcid.org/0000-0001-8704-8688;
Xiaojing Zheng https://orcid.org/0000-0002-6845-2949.

Appendix A. Validation of the solver

The numerical implementation is validated by comparing the statistics of the simulated single-phase (unladen) and particle-laden flows with those of the DNS database provided by Lee & Moser (2015) and Marchioli *et al.* (2008), at the same parameters. The single-phase flow is simulated at $Re_\tau = 550$, while the flows laden with uncharged particles (i.e. $q = 0$) are simulated at $Re_\tau = 150$ for three viscous aerodynamic Stokes numbers, $St^+ = 1$, 10, and 25. The former case is performed using the grid parameters shown in table 1, and the latter cases are carried out with the same parameters as in Marchioli *et al.* (2008). The comparisons of our simulated mean and root-mean-square (r.m.s.) velocities of the fluid and particle with the DNS database are shown in figures 20 and 21, respectively. It is clear that both the statistics of the simulated fluid and particle velocity agree well with those of the DNS database, thus validating our Eulerian–Lagrangian solver in a quantitative manner.

Appendix B. Shannon entropy

All simulations are initialized with randomly distributed particles, which are subsequently migrated towards the wall due to turbophoresis until a statistically steady state is reached. Herein, the Shannon entropy, which represents a global feature of the particle distribution at a instant (Picano, Sardina & Casciola 2009; Sardina *et al.* 2012; Motoori *et al.* 2022), is

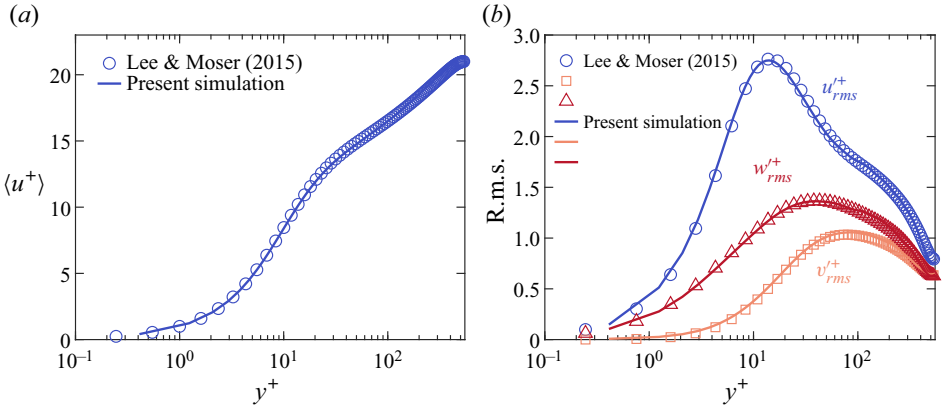

Figure 20. Comparison of our simulated single-phase velocity field with the results of Lee & Moser (2015) at $Re_\tau = 550$. (*a*) Wall-normal profiles of the mean streamwise velocity $\langle u^+ \rangle$. (*b*) Wall-normal profiles of the r.m.s. streamwise (u'^+_{rms}), wall-normal (v'^+_{rms}) and spanwise (w'^+_{rms}) velocity fluctuations. Here, lines denote the results of the present simulation, while open symbols denote those of Lee & Moser (2015).

defined as

$$S = -\sum_{i}^{N_{slab}} \frac{N_i}{N} \log \frac{N_i}{N}, \tag{B1}$$

where the computational domain is divided evenly into $N_{slab} = 200$ wall-parallel slabs, N_i is the number of particles within the ith slab, and N is the total number of particles. The Shannon entropy can be normalized by its maximum value $S_{max} = \log N_{slab}$, i.e. $S^* = S/S_{max}$, thus varying from 0 (all particles are located in a single slab) to 1 (particles are distributed homogeneously).

Figure 22 shows the evolution of normalized Shannon entropy S^* for all cases listed in table 2. For the monodisperse cases, the convergence rates decrease with increasing electric charge. In contrast, even though the convergence rates of the heavier particles in the bidisperse cases behave similarly, those of lighter particles increase with electric charge. Overall, the statistically steady states are achieved after $t^+ \approx 2.7 \times 10^4$ for all simulated cases.

Appendix C. Derivation of the wall-normal profile of the particle number density considering electrostatic forces

A statistical approach for describing the inertial particle concentration in wall-bounded turbulent flows was first proposed by Williams (1958) and recently discussed in detail by Sikovsky (2014), Johnson (2020) and Johnson *et al.* (2020). In this study, such a statistical model based on a kinetic equation for particle distribution function is extended to include the electrostatic forces. Since the particulate phase in the turbulent channel flows is statistically homogeneous in the wall-parallel planes (i.e. the x- and z-directions), the particle statistics can be reduced to the one-dimensional formulation in the y-direction. Let $f_p(y, v_p; t)$ denote the single-point p.d.f. in the particle phase space of coordinates and velocities (y, v_p). With this definition, the particle number density $n(y; t)$ is given by

$$n(y; t) = n_0 \int_{\mathbb{R}} f_p(y, v_p; t)\, \mathrm{d}v_p, \tag{C1}$$

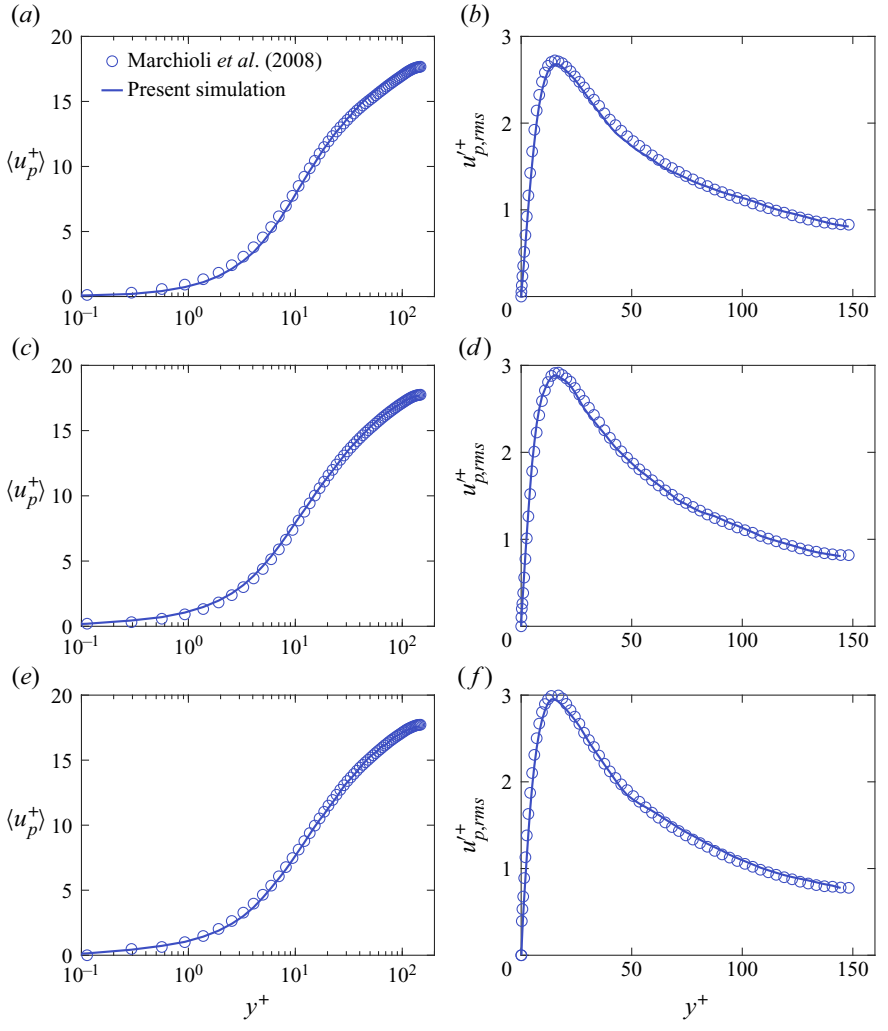

Figure 21. Comparison of our simulated particle velocity (in the case laden with uncharged particles) with the results of Marchioli *et al.* (2008) at $Re_\tau = 150$. (*a*,*b*) Wall-normal profiles of the mean streamwise particle velocity $\langle u_p^+ \rangle$ and the r.m.s. streamwise particle velocity fluctuations $u'^+_{p,rms}$ with Stokes number $St^+ = 1$. (*c*,*d*) Same as (*a*,*b*) but with $St^+ = 5$. (*e*,*f*) Same as (*a*,*b*) but with $St^+ = 25$. Here, lines denote the results of the present simulation, while open circles denote those of Marchioli *et al.* (2008).

where $n_0(t) = \int_{\mathbb{R}} n(y; t)\,\mathrm{d}y/L_y$ is the bulk particle number density. For any particle quantity $\psi_p(y, v_p; t)$, its conditional average (expectation) at position y and time t is defined as

$$\langle \psi_p | y \rangle = \frac{\displaystyle\int_{\mathbb{R}} \psi_p(y, v_p; t) f_p(y, v_p; t)\,\mathrm{d}v_p}{\displaystyle\int_{\mathbb{R}} f_p(y, v_p; t)\,\mathrm{d}v_p}, \tag{C2}$$

which leads to

$$\langle \psi_p | y \rangle n = n_0 \int_{\mathbb{R}} \psi_p(y, v_p; t) f_p(y, v_p; t)\,\mathrm{d}v_p. \tag{C3}$$

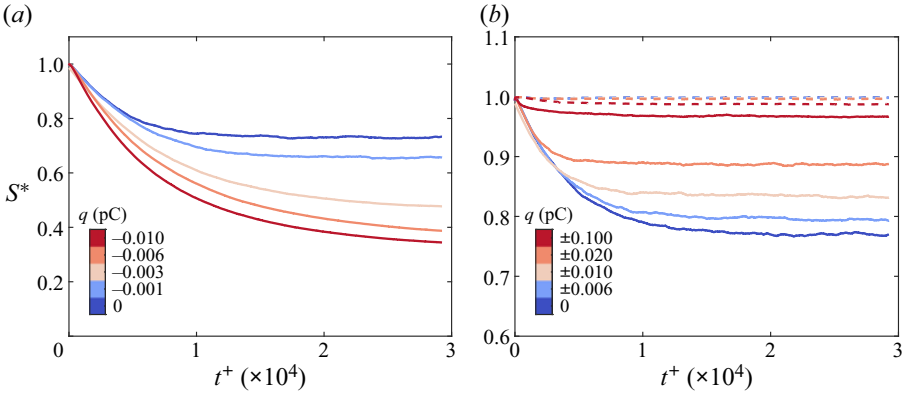

Figure 22. (*a*) Temporal evolution of the normalized Shannon entropy of particle distribution S^* for the monodisperse cases. (*b*) Same as (*a*) but for the bidisperse cases, where the solid and dashed lines denote the lighter ($St^+ = 20$) and heavier ($St^+ = 400$) particles, respectively.

Differentiating $f_p(y, v_p; t)$ with respect to time, one can obtain the evolution equation for $f_p(y, v_p; t)$:

$$\frac{\partial f_p}{\partial t} + \frac{\partial (v_p f_p)}{\partial y} + \frac{\partial (a_{p,y} f_p)}{\partial v_p} = \left(\frac{\partial f_p}{\partial t}\right)_{coll}, \tag{C4}$$

where $a_{p,y} = \mathrm{d}v_p/\mathrm{d}t$ is the particle acceleration, and $(\partial f_p/\partial t)_{coll}$ indicates the changes in $f_p(y, v_p; t)$ due to particle–particle collisions.

Multiplying (C4) by n_0 and v_p, and integrating over v_p while keeping in mind that the turbulence is statistically stationary (i.e. $\partial()/\partial t = 0$), we have

$$\frac{\mathrm{d}(\langle v_p^2|y\rangle\, n)}{\mathrm{d}y} - \langle a_{p,y}|y\rangle\, n = 0. \tag{C5}$$

Here, the collisional term $(\partial f_p/\partial t)_{coll}$ vanishes because particle–particle collisions conserve momentum.

Taking into account (2.5) and using the relation $\langle v_p|y\rangle = 0$ for mass conservation of the particulate phase (e.g. Johnson *et al.* 2020), (C5) can be rewritten as

$$\langle v_p^2|y\rangle \frac{\mathrm{d}n}{\mathrm{d}y} = \left(\frac{\langle \zeta\, v_{f@p}|y\rangle}{\tau_p} + \frac{q\,\langle E_{y@p}|y\rangle}{m_p} - \frac{\mathrm{d}\langle v_p^2|y\rangle}{\mathrm{d}y}\right) n. \tag{C6}$$

The solution of this ordinary differential equation for particle number density can be expressed explicitly as

$$n(y; t) = C \exp\left(\underbrace{\frac{1}{\tau_p}\int_0^y \frac{\langle \zeta\, v_{f@p}|\xi\rangle}{\langle v_p^2|\xi\rangle}\,\mathrm{d}\xi}_{\textit{biased sampling}}\right.$$

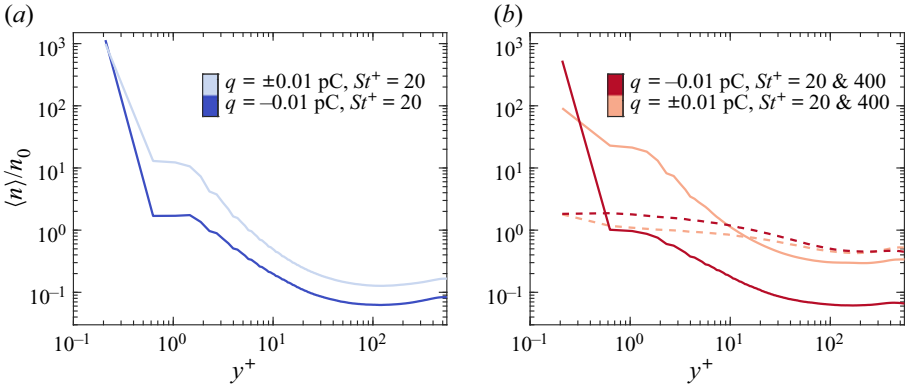

Figure 23. (*a*) Comparisons of the mean particle number densities for the cases MD0.01 (dark blue) and MD$^{\pm}$0.01 (light blue). (*b*) Same as (*a*) but for the cases BD$^{\pm}$0.01 (light red) and BD0.01 (dark red).

$$+ \underbrace{\frac{q}{m_p}\int_0^y \frac{\langle E_{y@p}|\xi\rangle}{\langle v_p^2|\xi\rangle}\,\mathrm{d}\xi}_{\textit{electrostatic forces}} - \underbrace{\int_0^y \frac{\mathrm{d}\ln\langle v_p^2|\xi\rangle}{\mathrm{d}\xi}\,\mathrm{d}\xi}_{\textit{turbophoresis}}\Bigg), \tag{C7}$$

where C is a constant of integration and vanishes when normalized by the bulk particle number density. Notably, for the bidisperse cases, the momentum exchanges between the lighter and heavier particles (inter-class interaction) are negligible at a relatively low particle volume fraction. In such a case, (C7) can be applied to each class of particles in the bidisperse cases. In (C7), the three terms on the right-hand side account for the effects of biased sampling of fluid velocity by particles (i.e. preferential concentration), electrostatic forces acting on particles, and turbophoresis, respectively. In practice, the conditional average $\langle\cdot|\xi\rangle$ is obtained by averaging over all particles within a horizontal layer centred at $y = \xi$. Also, time averaging of $n(y; t)$ is performed to obtain converged particle concentration $\langle n\rangle$.

Appendix D. Two complementary cases

In this appendix, we present two complementary simulations as a baseline case for comparison. The first simulation, referred to as MD$^{\pm}$0.01, consists of two groups of monodisperse particles with the same amounts but opposite signs of electrical charge, $q = \pm 0.01$ pC. The second simulation, referred to as BD0.01, comprises bidisperse particles with identical electrical charge $q = -0.01$ pC.

We compare the mean particle number density, mean particle streamwise velocity, r.m.s. particle fluctuating velocities, p.d.f.s of the normalized Voronoï areas, and ADFs of the lighter particles among the cases MD0.01, MD$^{\pm}$0.01, BD$^{\pm}$0.01 and BD0.01 in figures 23–26, respectively. As shown in figure 23, in the bulk of the channel, the number density of the lighter particles for the MD0.01 (BD0.01) case is lower than that for the MD$^{\pm}$0.01 (BD$^{\pm}$0.01) case. This occurs because in the 'monopolar' case, the electrostatic drift pushes the lighter particles towards the wall, while in the 'bipolar' case, it is directed towards the channel's centreline in the bulk of the channel. However, for the heavier particles, the number density in the BD0.01 case is higher than that in the BD$^{\pm}$0.01 case, implying a stronger wall-pointing electrostatic drift compared to the BD$^{\pm}$0.01 case.

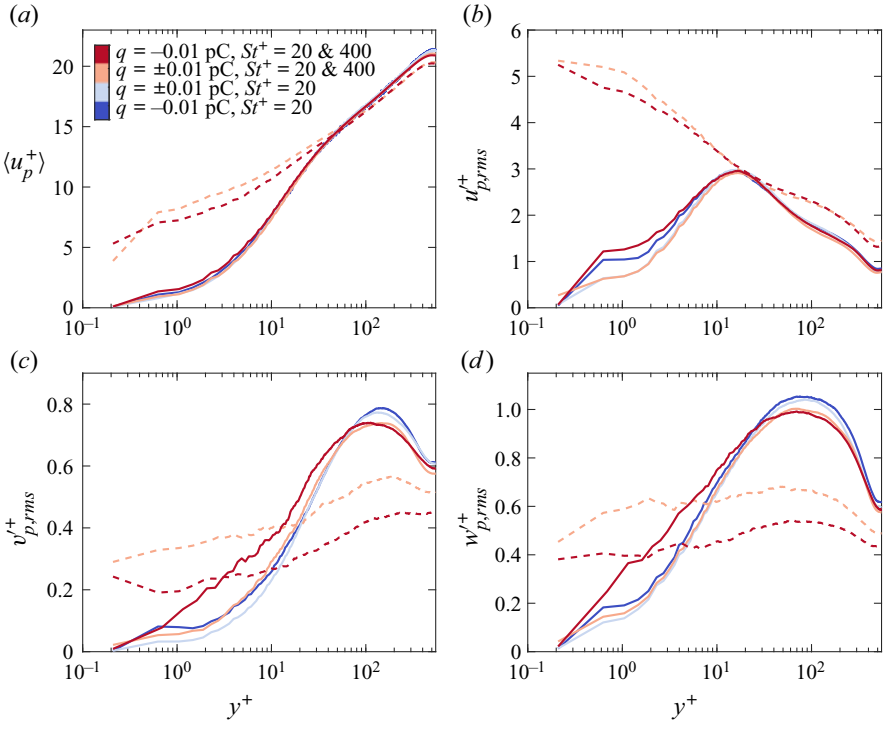

Figure 24. (*a*) Comparisons of the mean particle streamwise velocities between the cases MD0.01 (dark blue), MD$^{\pm}$0.01 (light blue), BD$^{\pm}$0.01 (light red) and BD0.01 (dark red). (*b–d*) Same as (*a*) but for the r.m.s. streamwise, wall-normal and spanwise particle fluctuating velocities, respectively.

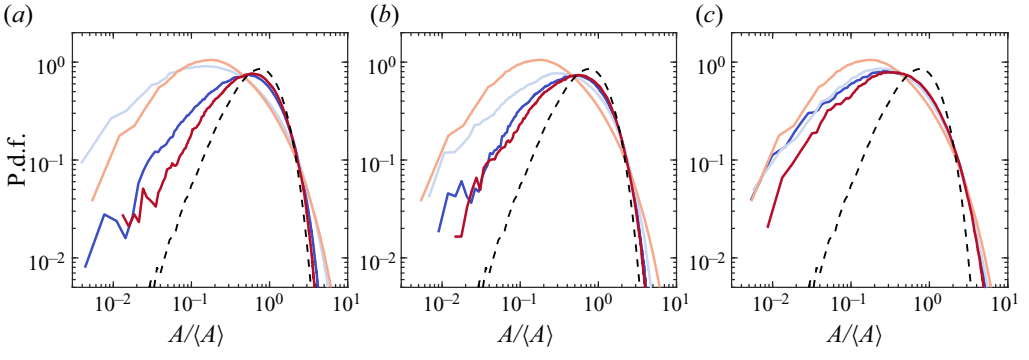

Figure 25. Comparisons of the p.d.f.s of the normalized Voronoï areas $A/\langle A\rangle$ between the cases MD0.01 (dark blue), MD$^{\pm}$0.01 (light blue), BD$^{\pm}$0.01 (light red) and BD0.01 (dark red) in three layers: (*a*) $y^+ \in [2.1, 5.6]$, (*b*) $y^+ \in [15.2, 25.0]$, and (*c*) $y^+ \in [530.5, 548.5]$ (same legend as figure 24).

Figure 24(*a*) shows that the mean particle streamwise velocity of the lighter particles is almost the same for different cases, while that of heavier particles is small for the MD0.01 case compared to the MD$^{\pm}$0.01 case. The r.m.s. particle fluctuating velocity exhibits a similar tendency for the heavier particles, but there is a slight variation for the lighter particles (figures 24*b–d*). In the MD0.01 (BD0.01) case, the lighter particles are distributed more uniformly compared to the MD$^{\pm}$0.01 (BD$^{\pm}$0.01) case (figure 25). This trend is consistent with the findings of figure 23 and can be attributed to the variations in particle

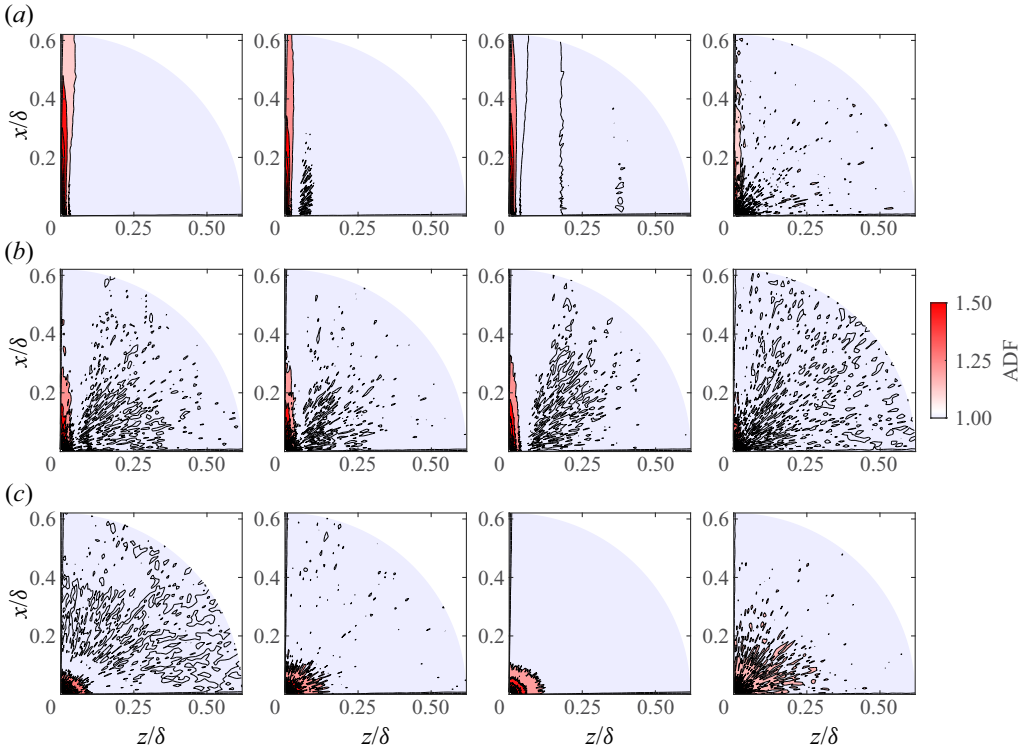

Figure 26. (*a*) Comparisons of the ADFs of the lighter particles in the layer $y^+ \in [2.1, 5.6]$ for various cases. Left-to-right: corresponding to the cases MD0.01, MD$^{\pm}$0.01, BD$^{\pm}$0.01 and BD0.01. (*b*,*c*) Same as (*a*) but for the particles in the layers $y^+ \in [15.2, 25.0]$ and [530.5, 548.5], respectively.

concentration. Furthermore, while the ADFs of the lighter particles in the MD$^{\pm}$0.01 case are nearly identical to those in the MD0.01 case, the spatial patterns of the ADFs in the BD0.01 case are weakened significantly in comparison to the BD$^{\pm}$0.01 case (figure 26).

References

Alipchenkov, V.M., Zaichik, L.I. & Petrov, O.F. 2004 Clustering of charged particles in isotropic turbulence. *High Temp.* **42**, 919–927.

Apte, S.V., Oujia, T., Matsuda, K., Kadoch, B., He, X. & Schneider, K. 2022 Clustering of inertial particles in turbulent flow through a porous unit cell. *J. Fluid Mech.* **937**, A9.

Arcen, B., Tanière, A. & Oesterlé, B. 2006 On the influence of near-wall forces in particle-laden channel flows. *Intl J. Multiphase Flow* **32**, 1326–1339.

Armenio, V. & Fiorotto, V. 2001 The importance of the forces acting on particles in turbulent flows. *Phys. Fluids* **13**, 2437–2440.

Aurenhammer, F. 1991 Voronoi diagrams – a survey of a fundamental geometric data structure. *ACM Comput. Surv.* **23**, 345–405.

Balachandar, S. 2009 A scaling analysis for point-particle approaches to turbulent multiphase flows. *Intl J. Multiphase Flow* **35**, 801–810.

Balachandar, S. & Eaton, J.K. 2010 Turbulent dispersed multiphase flow. *Annu. Rev. Fluid Mech.* **42**, 111–133.

Boutsikakis, A., Fede, P. & Simonin, O. 2022 Effect of electrostatic forces on the dispersion of like-charged solid particles transported by homogeneous isotropic turbulence. *J. Fluid Mech.* **938**, A33.

Brandt, L. & Coletti, F. 2022 Particle-laden turbulence: progress and perspectives. *Annu. Rev. Fluid Mech.* **54**, 159–189.

CAPECELATRO, J. & DESJARDINS, O. 2013 An Euler–Lagrange strategy for simulating particle-laden flows. *J. Comput. Phys.* **238**, 1–31.

CAPORALONI, M., TAMPIERI, F., TROMBETTI, F. & VITTORI, O. 1975 Transfer of particles in nonisotropic air turbulence. *J. Aerosol Sci.* **32**, 565–568.

CIMARELLI, C., ALATORRE-IBARGÜENGOITIA, M.A., KUEPPERS, U., SCHEU, B. & DINGWELL, D.B. 2014 Experimental generation of volcanic lightning. *Geology* **42**, 79–82.

COSTA, P. 2018 A FFT-based finite-difference solver for massively-parallel direct numerical simulations of turbulent flows. *Comput. Maths Applics.* **76**, 1853–1862.

COSTA, P., BRANDT, L. & PICANO, F. 2020 Interface-resolved simulations of small inertial particles in turbulent channel flow. *J. Fluid Mech.* **883**, A54.

DI RENZO, M., JOHNSON, P.L., BASSENNE, M., VILLAFAÑE, L. & URZAY, J. 2019 Mitigation of turbophoresis in particle-laden turbulent channel flows by using incident electric fields. *Phys. Rev. Fluids* **4**, 124303.

DI RENZO, M. & URZAY, J. 2018 Aerodynamic generation of electric fields in turbulence laden with charged inertial particles. *Nat. Commun.* **9**, 1676.

DRITSELIS, C.D. & VLACHOS, N.S. 2008 Numerical study of educed coherent structures in the near-wall region of a particle-laden channel flow. *Phys. Fluids* **20**, 055103.

EATON, J.K. & FESSLER, J. 1994 Preferential concentration of particles by turbulence. *Intl J. Multiphase Flow* **20**, 169–209.

FERENC, J.S. & NÉDA, Z. 2007 On the size distribution of Poisson Voronoi cells. *Physica* A **385**, 518–526.

FONG, K.O., AMILI, O. & COLETTI, F. 2019 Velocity and spatial distribution of inertial particles in a turbulent channel flow. *J. Fluid Mech.* **872**, 367–406.

GAO, W., SAMTANEY, R. & RICHTER, D.H. 2023 Direct numerical simulation of particle-laden flow in an open channel at $Re_\tau = 5186$. *J. Fluid Mech.* **957**, A3.

GONDRET, P., LANCE, M. & PETIT, L. 2002 Bouncing motion of spherical particles in fluids. *Phys. Fluids* **14**, 643–652.

GROSSHANS, H., BISSINGER, C., CALERO, M. & PAPALEXANDRIS, M.V. 2021 The effect of electrostatic charges on particle-laden duct flows. *J. Fluid Mech.* **909**, A21.

GROSSHANS, H. & PAPALEXANDRIS, M.V. 2016 Large eddy simulation of triboelectric charging in pneumatic powder transport. *Powder Technol.* **301**, 1008–1015.

GROSSHANS, H. & PAPALEXANDRIS, M.V. 2017*a* Direct numerical simulation of triboelectric charging in particle-laden turbulent channel flows. *J. Fluid Mech.* **818**, 465–491.

GROSSHANS, H. & PAPALEXANDRIS, M.V. 2017*b* On the accuracy of the numerical computation of the electrostatic forces between charged particles. *Powder Technol.* **322**, 185–194.

HAMAMOTO, N., NAKAJIMA, Y. & SATO, T. 1992 Experimental discussion on maximum surface charge density of fine particles sustainable in normal atmosphere. *J. Electrostat.* **28**, 161–173.

HORWITZ, J.A.K. & MANI, A. 2016 Accurate calculation of Stokes drag for point-particle tracking in two-way coupled flows. *J. Comput. Phys.* **318**, 85–109.

JIE, Y., CUI, Z., XU, C. & ZHAO, L. 2022 On the existence and formation of multi-scale particle streaks in turbulent channel flows. *J. Fluid Mech.* **935**, A18.

JOHNSON, P.L. 2020 Predicting the impact of particle–particle collisions on turbophoresis with a reduced number of computational particles. *Intl J. Multiphase Flow* **124**, 103182.

JOHNSON, P.L., BASSENNE, M. & MOIN, P. 2020 Turbophoresis of small inertial particles: theoretical considerations and application to wall-modelled large-eddy simulations. *J. Fluid Mech.* **883**, A27.

JOSEPH, G.G., ZENIT, R., HUNT, M.L. & ROSENWINKEL, A.M. 2001 Particle–wall collisions in a viscous fluid. *J. Fluid Mech.* **433**, 329–346.

KARNIK, A.U. & SHRIMPTON, J.S. 2012 Mitigation of preferential concentration of small inertial particles in stationary isotropic turbulence using electrical and gravitational body forces. *Phys. Fluids* **24**, 073301.

KIM, J. & MOIN, P. 1985 Application of a fractional-step method to incompressible Navier–Stokes equations. *J. Comput. Phys.* **59**, 308–323.

KOK, J.F. & RENNO, N.O. 2006 Enhancement of the emission of mineral dust aerosols by electric forces. *Geophys. Res. Lett.* **33**, L19S10.

KOLEHMAINEN, J., OZEL, A., BOYCE, C.M. & SUNDARESAN, S. 2016 A hybrid approach to computing electrostatic forces in fluidized beds of charged particles. *AIChE J.* **62**, 2282–2295.

KOLEHMAINEN, J., OZEL, A. & SUNDARESAN, S. 2018 Eulerian modelling of gas–solid flows with triboelectric charging. *J. Fluid Mech.* **848**, 340–369.

KULICK, J.D., FESSLER, J.R. & EATON, J.K. 1994 Particle response and turbulence modification in fully developed channel flow. *J. Fluid Mech.* **277**, 109–134.

LACKS, D.J. & SANKARAN, R.M. 2011 Contact electrification of insulating materials. *J. Phys.* D*: Appl. Phys.* **44**, 453001.

LAVRINENKO, A., FABREGAT, A. & PALLARES, J. 2022 Comparison between fully resolved and time-averaged simulations of particle cloud dispersion produced by a violent expiratory event. *Acta Mechanica Sin.* **38**, 721489.

LEE, M. & MOSER, R.D. 2015 Direct numerical simulation of turbulent channel flow up to $Re_\tau \approx 5200$. *J. Fluid Mech.* **774**, 395–415.

LI, J., WANG, H., LIU, Z., CHEN, S. & ZHENG, C. 2012 An experimental study on turbulence modification in the near-wall boundary layer of a dilute gas–particle channel flow. *Exp. Fluids* **53**, 1385–1403.

LIU, Y., SHEN, L., ZAMANSKY, R. & COLETTI, F. 2020 Life and death of inertial particle clusters in turbulence. *J. Fluid Mech.* **902**, R1.

LU, J., NORDSIEK, H., SAW, E.W. & SHAW, R.A. 2010 Clustering of charged inertial particles in turbulence. *Phys. Rev. Lett.* **104**, 184505.

LU, J. & SHAW, R.A. 2015 Charged particle dynamics in turbulence: theory and direct numerical simulations. *Phys. Fluids* **27**, 065111.

MARCHIOLI, C. & SOLDATI, A. 2002 Mechanisms for particle transfer and segregation in a turbulent boundary layer. *J. Fluid Mech.* **468**, 283–315.

MARCHIOLI, C., SOLDATI, A., KUERTEN, J.G.M., ARCEN, B., TANIERE, A., GOLDENSOPH, G., SQUIRES, K.D., CARGNELUTTI, M.F. & PORTELA, L.M. 2008 Statistics of particle dispersion in direct numerical simulations of wall-bounded turbulence: results of an international collaborative benchmark test. *Intl J. Multiphase Flow* **34**, 879–893.

MARSHALL, J.S. 2009 Discrete-element modeling of particulate aerosol flows. *J. Comput. Phys.* **228**, 1541–1561.

MATHER, T.A. & HARRISON, R.G. 2006 Electrification of volcanic plumes. *Surv. Geophys.* **27**, 387–432.

MAXEY, M.R. 1987 The gravitational settling of aerosol particles in homogeneous turbulence and random flow fields. *J. Fluid Mech.* **174**, 441–465.

MAXEY, M.R. & RILEY, J.J. 1983 Equation of motion for a small rigid sphere in a nonuniform flow. *Phys. Fluids* **26**, 883–889.

MÉNDEZ HARPER, J. & DUFEK, J. 2016 The effects of dynamics on the triboelectrification of volcanic ash. *J. Geophys. Res.: Atmos.* **121**, 8209–8228.

MONCHAUX, R., BOURGOIN, M. & CARTELLIER, A. 2010 Preferential concentration of heavy particles: a Voronoï analysis. *Phys. Fluids* **22**, 103304.

MONCHAUX, R., BOURGOIN, M. & CARTELLIER, A. 2012 Analyzing preferential concentration and clustering of inertial particles in turbulence. *Intl J. Multiphase Flow* **40**, 1–18.

MOTOORI, Y., WONG, C. & GOTO, S. 2022 Role of the hierarchy of coherent structures in the transport of heavy small particles in turbulent channel flow. *J. Fluid Mech.* **942**, A3.

NIFUKU, M. & KATOH, H. 2003 A study on the static electrification of powders during pneumatic transportation and the ignition of dust cloud. *Powder Technol.* **135**, 234–242.

NINTO, Y. & GARCIA, M.H. 1996 Experiments on particle–turbulence interactions in the near-wall region of an open channel flow: implications for sediment transport. *J. Fluid Mech.* **326**, 285–319.

OKA, S. & GOTO, S. 2021 Generalized sweep-stick mechanism of inertial-particle clustering in turbulence. *Phys. Rev. Fluids* **6**, 044605.

OUJIA, T., MATSUDA, K. & SCHNEIDER, K. 2020 Divergence and convergence of inertial particles in high-Reynolds-number turbulence. *J. Fluid Mech.* **905**, A14.

PAN, Y. & BANERJEE, S. 1996 Numerical simulation of particle interactions with wall turbulence. *Phys. Fluids* **8**, 2733–2755.

PAN, Y. & BANERJEE, S. 1997 Numerical investigation of the effects of large particles on wall-turbulence. *Phys. Fluids* **9**, 3786–3807.

PEDINOTTI, S., MARIOTTI, G. & BANERJEE, S. 1992 Direct numerical simulation of particle behaviour in the wall region of turbulent flows in horizontal channels. *Intl J. Multiphase Flow* **18**, 927–941.

PETERSEN, A.J., BAKER, L. & COLETTI, F. 2019 Experimental study of inertial particles clustering and settling in homogeneous turbulence. *J. Fluid Mech.* **864**, 925–970.

PICANO, F., SARDINA, G. & CASCIOLA, C.M. 2009 Spatial development of particle-laden turbulent pipe flow. *Phys. Fluids* **21**, 093305.

REEKS, M.W. 1983 The transport of discrete particles in inhomogeneous turbulence. *J. Aerosol Sci.* **14**, 729–739.

RENNO, N.O. & KOK, J.F. 2008 Electrical activity and dust lifting on Earth, Mars, and beyond. *Space Sci. Rev.* **137**, 419–434.

RICE, M.A., WILLETTS, B.B. & MCEWAN, I.K. 1995 An experimental study of multiple grain-size ejecta produced by collisions of saltating grains with a flat bed. *Sedimentology* **42**, 695–706.

RUDGE, W.D. 1913 Atmospheric electrification during South African dust storms. *Nature* **91**, 31–32.

SARDINA, G., PICANO, F., SCHLATTER, P., BRANDT, L. & CASCIOLA, C.M. 2011 Large scale accumulation patterns of inertial particles in wall-bounded turbulent flow. *Flow Turbul. Combust.* **86**, 519–532.

SARDINA, G., SCHLATTER, P., BRANDT, L., PICANO, F. & CASCIOLA, C.M. 2012 Wall accumulation and spatial localization in particle-laden wall flows. *J. Fluid Mech.* **699**, 50–78.

SCHILLER, L. & NAUMANN, A. 1935 A drag coefficient correlation. *Z. Verein. Deutsch. Ing.* **77**, 318–320.

SCHMIDT, D.S., SCHMIDT, R.A. & DENT, J.D. 1998 Electrostatic force on saltating sand. *J. Geophys. Res.: Atmos.* **103**, 8997–9001.

SCHUMANN, U. & SWEET, R.A. 1988 Fast Fourier transforms for direct solution of Poisson's equation with staggered boundary conditions. *J. Comput. Phys.* **75**, 123–137.

SIKOVSKY, D.P. 2014 Singularity of inertial particle concentration in the viscous sublayer of wall-bounded turbulent flows. *Flow Turbul. Combust.* **92**, 41–64.

SIPPOLA, P., KOLEHMAINEN, J., OZEL, A., LIU, X., SAARENRINNE, P. & SUNDARESAN, S. 2018 Experimental and numerical study of wall layer development in a tribocharged fluidized bed. *J. Fluid Mech.* **849**, 860–884.

SOLDATI, A. & MARCHIOLI, C. 2009 Physics and modelling of turbulent particle deposition and entrainment: review of a systematic study. *Intl J. Multiphase Flow* **35**, 827–839.

TAGAWA, Y., MERCADO, J.M., PRAKASH, V.N., CALZAVARINI, E., SUN, C. & LOHSE, D. 2012 Three-dimensional Lagrangian Voronoï analysis for clustering of particles and bubbles in turbulence. *J. Fluid Mech.* **693**, 201–215.

UHLMANN, M. & DOYCHEV, T. 2014 Sedimentation of a dilute suspension of rigid spheres at intermediate Galileo numbers: the effect of clustering upon the particle motion. *J. Fluid Mech.* **752**, 310–348.

VANCE, M.W., SQUIRES, K.D. & SIMONIN, O. 2006 Properties of the particle velocity field in gas–solid turbulent channel flow. *Phys. Fluids* **18**, 063302.

WALLACE, J.M., ECKELMANN, H. & BRODKEY, R.S. 1972 The wall region in turbulent shear flow. *J. Fluid Mech.* **54**, 39–48.

WANG, G., FONG, K.O., COLETTI, F., CAPECELATRO, J. & RICHTER, D.H. 2019 Inertial particle velocity and distribution in vertical turbulent channel flow: a numerical and experimental comparison. *Intl J. Multiphase Flow* **120**, 103105.

WANG, G. & RICHTER, D.H. 2019 Two mechanisms of modulation of very-large-scale motions by inertial particles in open channel flow. *J. Fluid Mech.* **868**, 538–559.

WANG, L.P., WEXLER, A.S. & ZHOU, Y. 2000 Statistical mechanical description and modelling of turbulent collision of inertial particles. *J. Fluid Mech.* **415**, 117–153.

WILLIAMS, F.A. 1958 Spray combustion and atomization. *Phys. Fluids* **1**, 541–545.

YAIR, Y., KATZ, S., YANIV, R., ZIV, B. & PRICE, C. 2016 An electrified dust storm over the Negev Desert, Israel. *Atmos. Res.* **181**, 63–71.

YAMAMOTO, Y., POTTHOFF, M., TANAKA, T., KAJISHIMA, T. & TSUJI, Y. 2001 Large-eddy simulation of turbulent gas–particle flow in a vertical channel: effect of considering inter-particle collisions. *J. Fluid Mech.* **442**, 303–334.

YANG, F.L. & HUNT, M.L. 2006 Dynamics of particle–particle collisions in a viscous liquid. *Phys. Fluids* **18**, 121506.

YAO, Y. & CAPECELATRO, J. 2018 Competition between drag and Coulomb interactions in turbulent particle-laden flows using a coupled-fluid-Ewald-summation based approach. *Phys. Rev. Fluids* **3**, 034301.

ZHANG, H. & ZHENG, X. 2018 Quantifying the large-scale electrification equilibrium effects in dust storms using field observations at Qingtu Lake Observatory. *Atmos. Chem. Phys.* **18**, 17087–17097.

ZHANG, H. & ZHOU, Y.H. 2020 Reconstructing the electrical structure of dust storms from locally observed electric field data. *Nat. Commun.* **11**, 5072.

ZHANG, H. & ZHOU, Y.H. 2023 Unveiling the spectrum of electrohydrodynamic turbulence in dust storms. *Nat. Commun.* **14**, 408.

ZHAO, L., ANDERSSON, H.I. & GILLISSEN, J.J. 2013 Interphasial energy transfer and particle dissipation in particle-laden wall turbulence. *J. Fluid Mech.* **715**, 32–59.

ZHENG, X.J. 2013 Electrification of wind-blown sand: recent advances and key issues. *Eur. Phys. J.* E **36**, 138.

ZHENG, X., FENG, S. & WANG, P. 2021 Modulation of turbulence by saltating particles on erodible bed surface. *J. Fluid Mech.* **918**, A16.

ZHENG, X.J., HUANG, N. & ZHOU, Y.H. 2003 Laboratory measurement of electrification of wind-blown sands and simulation of its effect on sand saltation movement. *J. Geophys. Res.: Atmos.* **108**, 4322.

ZHU, H., PAN, C., WANG, G., LIANG, Y., JI, X. & WANG, J. 2021 Attached eddy-like particle clustering in a turbulent boundary layer under net sedimentation conditions. *J. Fluid Mech.* **920**, A53.